UNIVERSITAT POLITÈCNICA DE CATALUNYA
BARCELONATECH
Escola d'Enginyeria de Telecomunicació
i Aeroespacial de Castelldefels

TREBALL DE FI DE GRAU

TFG TITLE: Application of Active Flow Control on airfoils at ultralow Reynolds numbers

DEGREE: Grau en Enginyeria d'Aeronavegació

AUTHOR: Carlos San Gabriel Romero

ADVISOR: Fernando Pablo Mellibovsky Elstein

DATE: October 19, 2019

Título: Application of Active Flow Control on airfoils at ultralow Reynolds numbers

Autor: Carlos San Gabriel Romero

Director: Fernando Pablo Mellibovsky Elstein

Fecha: 19 d'octubre de 2019

Resumen

En un estudio anterior las técnicas de control de flujo activo, como es el caso de los sweeping jets, aplicadas en un Reynolds ultra bajo (Re=1000) demostraron ser efectivas en cuanto al lift se refiere, pero las altas velocidades que provocan cerca de la superficie causaron a su vez un empeoramiento del drag de fricción.En este estudio, se han analizado primero las diferentes configuraciones de actuadores existentes con el objetivo de determinar los factores que más influyen en el aumento del drag viscoso. Después se han propuesto varias hipótesis con el objetivo de reducir el empeoramiento del drag manteniendo el incremento del lift. En este sentido, se ha decidido modificar la geometría de los actuadores usando dos parámetros de control; el ancho del jet y el ángulo en el cual se inyecta el fluido. Estas modificaciones se han aplicado a tres tipos de actuaciones; soplado, succión y synthetic jets. Para las simulaciones se ha usado un perfil NACA0012 2D, en el cual se ha modificado el mallado para poder incluir los cambios en la geometría. Los resultados obtenidos difieren según el tipo de actuación en el cual son aplicados. La modificación del ángulo del jet ha obtenido resultados interesantes en el caso del soplado, en el cual se ha encontrado un ángulo que maximiza el lift. En el caso del ancho del jet también se ha encontrado un valor óptimo para el coeficiente de momento utilizado, que además es aplicable para los tres tipos de actuaciones. En definitiva, se ha probado que a además del coeficiente de momento y la posición del actuador las características geométricas de los actuadores también juegan un papel destacable en la eficiencia de la actuación.

Title : Application of Active Flow Control on airfoils at ultralow Reynolds numbers

Author: Carlos San Gabriel Romero

Advisor: Fernando Pablo Mellibovsky Elstein

Date: October 19, 2019

Overview

In a previous research Active Flow Control techniques, such as sweeping jets, applied in an ultra-low Reynolds regime (Re=1000) were found effective to reattach an already separated flow achieving lift enhancements but also inducing a large skin-friction drag increase due to the high velocities near the airfoil surface. In this study, firstly the current actuator configurations have been analyzed with the objective of determining the most important factors involved in the increase of the viscous drag. Then, several hypothesis have been done with the aim of reducing this drag penalty while keeping the lift enhancement. The decision taken in this sense has been to apply geometrical modifications to the the actuators using two control parameters, the jet width and the jet angle in which the fluid is injected. Moreover these modifications have been applied to three different actuation types; blowing, suction and synthetic jets. The simulations have been carried in a 2D NACA0012 airfoil in which a remeshing has been done in order to apply the commented modifications. The obtained results show variations depending on in which actuation type are applied. The jet angle modification has obtained interesting results for the blowing jet, since an angle that maximizes the lift coefficient has been found. The jet width has also obtained an optimum value for a specific momentum coefficient, that moreover is suitable for the three actuations. In conclusion, it has been proved that that besides the momentum coefficient and the jet location the geometrical parameters of the actuator have also a considerable impact on the overall efficiency of the actuation.

CONTENTS

Introduction 1

CHAPTER 1. Theoretical background 3

1.1. Problem definition 3

1.2. High-lift devices 4

1.3. Flow control techniques 5

1.3.1. Passive Flow control 5

1.3.2. Active Flow control 7

CHAPTER 2. Assumptions of the study 11

2.1. Reynolds Number 11

2.1.1. Reynolds Number influence in the study 12

CHAPTER 3. Methodology 15

3.1. Simulation Pipeline 15

3.2. Softwares description 17

3.2.1. Nektar 17

3.2.2. GMSH 17

3.2.3. Clufa UPC 17

3.2.4. Paraview 17

3.2.5. Matlab 17

3.3. Mesh 18

3.3.1. Mesh geometry 18

3.3.2. Mesh discretization 20

3.4. Navier-Stokes Resolution 21

3.4.1. Spectral/hp element method 22

3.5. Solver configuration 23

3.5.1. Expansions 23

3.5.2. Solver information 23

3.5.3. Parameters 24

3.5.4. Boundary conditions 24

3.5.5. Filters . . . 25

3.6. Convergence study . . . 26

CHAPTER 4. Baseline Results . . . 29

4.1. Flow natural behaviour . . . 29

4.1.1. Baseline airfoil performance . . . 29

4.2. Baseline Actuation . . . 31

4.2.1. Streamwise-normal sweeping jet . . . 31

4.2.2. Streamwise Sweeping Jet . . . 32

CHAPTER 5. Simulation Results . . . 35

5.1. Mesh adaptation . . . 35

5.2. Jet Parametrisation . . . 36

5.3. Blowing Jet . . . 38

5.3.1. Jet width study . . . 38

5.3.2. Jet angle study . . . 45

5.3.3. Blowing jet results summary . . . 50

5.4. Suctioning Jet . . . 51

5.4.1. Jet width study . . . 52

5.4.2. Jet angle study . . . 52

5.5. Synthetic Jet . . . 57

5.5.1. Synthetic jet parametrisation . . . 57

5.5.2. Synthetic Jet results . . . 58

5.5.3. Synthetic jet comparison . . . 62

Conclusions . . . 63

Bibliography . . . 65

LIST OF FIGURES

1.1 Boundary layer detachment [1] . . . 3
1.2 Triple-slotted airfoil with slat [2] . . . 4
1.3 Velocity streamlines in double-slotted flap and slat [3] . . . 4
1.4 Comparison of averaged velocities in laminar and turbulent flow . . . 6
1.5 Vortex Generators on a Boeing 737-800 wing . . . 7
1.6 Three forms of flow control actuators [19] . . . 8
1.7 Schematic of a conventional curved sweeping jet [11] . . . 9
1.8 Schematic of a Synthetic Jet [20] . . . 9

2.1 Conventional airfoil separation characteristics at different Reynolds number regimes below 10^6 . . . 12
2.2 Influence of Reynolds number on airfoil NACA-0012 behaviour (Musial and Cromack, 1988) . . . 13

3.1 Schematic of the simulation pipeline . . . 16
3.2 Baseline c-mesh . . . 18
3.3 Mesh Regions . . . 19
3.4 Near-field region zoomed . . . 20
3.5 Solver Information for unsteady incompressible Navier-Stokes resolution . . . 24
3.6 Outlet Boundary conditions . . . 25
3.7 Xfoil results . . . 27

4.1 Baseline vorticity contour and streamlines . . . 29
4.2 Baseline wall shear stress for the maximum and minimum lift coefficient instants. 30
4.3 Baseline lift and drag coefficients time response . . . 30
4.4 Streamwise-normal sweeping jet [15] . . . 31
4.5 Streamwise sweeping jet [15] . . . 32

5.1 Jet slot geometry for a jet angle of 90^o . . . 36
5.2 Mesh adaptation for the new actuation . . . 36
5.3 CL vs Jet width . . . 39
5.4 CD vs Jet width . . . 39
5.5 Viscous and Pressure drag coefficient vs Jet width . . . 40
5.6 Vorticity contour and streamlines for jet width 0.3% and 1% actuation . . . 41
5.7 Jet width impact on the wall shear stress over airfoil upper surface . . . 42
5.8 Jet width impact on the pressure distribution over airfoil surface . . . 43
5.9 Detailed regions of the pressure distribution . . . 44
5.10 Lift coefficient variation with jet angle . . . 45
5.11 Pressure drag coefficient variation with jet angle . . . 46
5.12 Vorticity contour and streamlines for a jet angle of 60^o, 40^o and 30^o . . . 47
5.13 Jet angle impact on the wall shear stress over airfoil upper surface . . . 48
5.14 Jet angle impact on the pressure coefficient . . . 49
5.15 Vorticity contour and streamlines for a suctioning jet with 0.8% of jet width and 40^o of jet angle . . . 51

5.16 Jet angle impact on the lift coefficient . . . 53
5.17 Jet angle impact on the drag coefficient . . . 53
5.18 Vorticity contour and streamlines for a jet angle of 80° and 20°. Maximum lift coefficient instant. . . . 54
5.19 Jet angle impact on the pressure coefficient for a suctioning jet . . . 55
5.20 Pressure distribution zoom at the jet slot region . . . 55
5.21 Jet angle impact on the wall shear stress coefficient for a suctioning jet . . . 56
5.22 Lift coefficient time response for a synthetic jet with jet frequency f_o, jet angle 40° and jet width 0.8% . . . 59
5.23 Drag coefficient time response for a synthetic jet with jet frequency f_o, jet angle 40° and jet width 0.8% . . . 59
5.24 Lift coefficient time response for a synthetic jet with C_μ 1%, jet angle 40° and jet width 0.8% . . . 60
5.25 Drag coefficient time response for a synthetic jet with C_μ 1%, jet angle 40° and jet width 0.8% . . . 61
5.26 Lift coefficient time response for the three actuation in the study . . . 62

TABLES INDEX

3.1 Control Volume sizing 26
3.2 Expansions over the different composites 26
3.3 Accuracy comparison with Nektar++ 26

4.1 Baseline results 31
4.2 Streamwise-normal Sweeping jet best results and baseline comparison 32
4.3 Streamwise sweeping jet best results summary 33

5.1 Maximum jet output velocity U_{Jmax} for every jet width 38
5.2 Jet width influence on the baseline airfoil performance ($C_\mu = 0$) 38
5.3 Aerodynamic characteristics for the jet width study 50
5.4 Aerodynamic characteristics for the jet angle study 50
5.5 Aerodynamic characteristics for the suctioning jet study 52
5.6 Aerodynamic characteristics for a suctioning actuation with 0.8% and 0.5% of jet width and 40^o of jet angle 52
5.7 Aerodynamic characteristics for a suctioning actuation with 0.8% of jet angle . . 56
5.8 Momentum coefficient impact on the aerodynamic performance 60
5.9 Jet frequency impact on the aerodynamic characteristics for a synthetic jet . . . 61

INTRODUCTION

Airfoil wing profiles of most commercial aviation aircraft are designed to obtain its maximum performance and efficiency in cruise phase, where almost no angle of attack is needed and speed is in high subsonic or transonic regime. In take off and landing operations, where an increase of lift is needed, we are far from these design conditions and therefore the use of high-lift devices such as flaps and slats is required.

In this project we will focus on the use of Active Flow Control techniques as a method to overcome the necessity of high-lift devices involving moving parts, as they are subject to mechanical failures and add extra weight due to its redundant control systems.

Previous research [15] has shown that momentum injection to the boundary layer in the form of a periodic excitation can prevent or retard flow detachment as well as reattach an already separated flow. Two main techniques have been studied, sweeping jets that are based on steady and unsteady blowing and zero-net-mass-flux actuators called synthetic jets. Both types of fluidic actuators have provided interesting results in terms of lift enhancement but the high velocities induced near the wall results also in large skin-friction drag increase.

In this study we start from ongoing research with the aim of optimising and thus improving the aerodynamic efficiency of this type of fluidic actuation. First we will assess the dependence of skin-friction drag on the various parameters that determine the actuator momentum coefficient in order to isolate the most important factors. Then we will try different configurations and shapes of fluidic actuators, in particular synthetic jets and sweeping jets, with the objective of reducing momentum coefficient as well as total and viscous drag while keeping lift enhancement.

CHAPTER 1. THEORETICAL BACKGROUND

1.1. Problem definition

As it was previously commented during the introduction section in take off and landing operations the thin and almost camber-less airfoil wing profiles designed for cruising flight become inefficient when exposed to higher angles of attack, where an increased thickness and camber would be desirable. At this off-design conditions airfoils may suffer what is called boundary layer detachment, a physical phenomenon that occurs when an adverse pressure gradient forces the separation of the fluid layer flowing in the immediate vicinity of the airfoil surface thus producing a region of recirculated flow.

This recirculation can be basically explained by the pressure conditions existing over the airfoil's surface and also taking into account viscous and friction effects. In the following figure 1.1 two useful separation cases to understand the physics related to problem are represented.

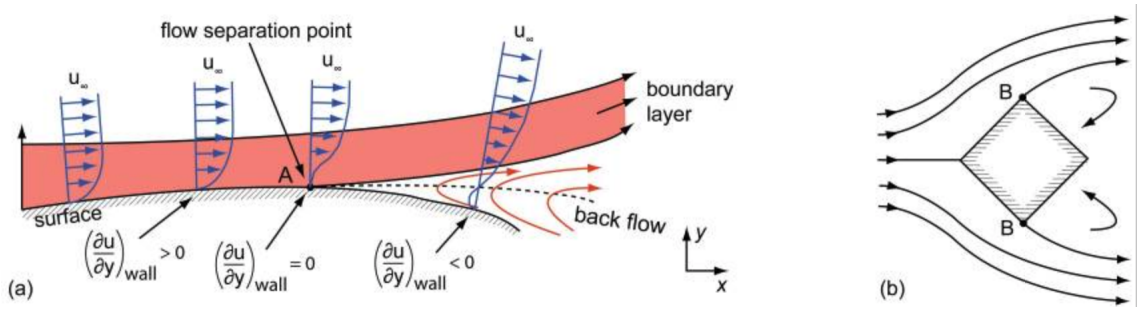

Figure 1.1: Boundary layer detachment [1]

In figure1.1(a), the viscous friction has the fluid adhered to the airfoil surface (no-slip condition), generating a thin fluid layer, with velocities lower than in the outer flow, it is called the boundary layer. Taking into account the pressure distribution over an airfoil, the boundary layer when subject to adverse pressure gradients as is the case at the rear of airfoils, loses the already defective momentum and separates producing a recirculated flow region beyond the separation point. This situation is aggravated when the angle of attack is increased, which is translated into an increase of pressure at the trailing edge and in consequence higher adverse pressure gradients.

In figure 1.1(b) the separation mechanism is the same but it is visually more evident. At point B the adverse pressure gradient is very large at a precise location due to the kink in the geometry, in addition the increase of the section at this region decreases the velocity following mass conservation law and thus increasing the pressure what again forces a separation and a back flow.

1.2. High-lift devices

The consequences of boundary layer detachment are varied, some of them affect negatively to the flight performance and could even compromise in-flight safety. An abrupt decrease of lift is experienced since there is a reduction of flow velocity in the upper surface. Drag also suffers a noticeable increase caused by the increased pressure on rear's airfoil, this leads to an increase of pressure drag, whereas skin-friction drag evidently decreases due to the flow separation. This situation can lead an aircraft to enter in "stall", that is an undesirable situation in which weight exceeds total lift. The most extended solution that has been used almost since the beginning of aviation's history is the use of high-lift devices such as flaps and slats. The effectiveness of this devices relies on the modification of wing's geometry and area by the deployment of the leading edge (slats) or the trailing edge (flaps), they are shown in figure 1.2.

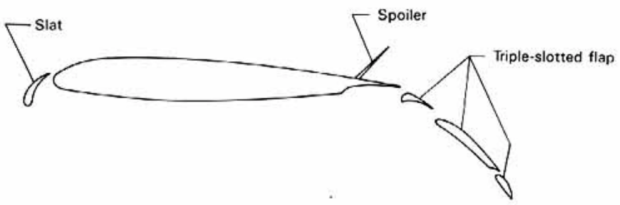

Figure 1.2: Triple-slotted airfoil with slat [2]

Leading-edge devices are basically designed to assist the flow in negotiating the sharp turn from the lower surface around the leading edge, preventing early flow separation. A slot between the slat and the main airfoil is a configuration that helps the flow to stay attached over the surface preventing a transition from laminar to turbulent (as shown in figure 1.3(b)), due to its increased flow velocity [2].

Trailing-edge devices are designed to increase the effective angle in which the flow is turned and thus increase the lifting capability. There are different flap configurations depending on the number of devices, but its real effectiveness relies also in the slot preceding the flap. In figure 1.3 the flow through the slot energizes the boundary layer on the top surface, which is negotiating an adverse pressure gradient, and thus prevents separation and the subsequent loss of lift [3].

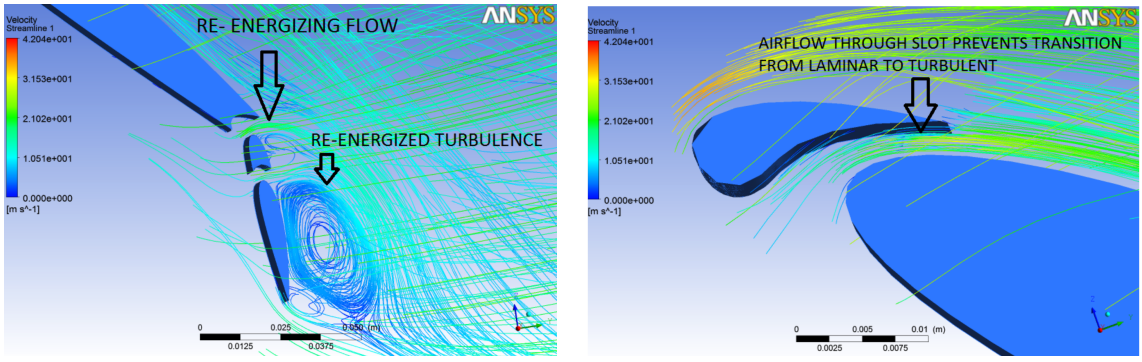

(a) Double-slotted flap (b) Slat

Figure 1.3: Velocity streamlines in double-slotted flap and slat [3]

Both devices, flaps and slats, are fully retracted in cruising flight but take up a considerable room inside the wings, where fuel is stored. In addition, they add weight and parasitic drag due to its mechanical mechanism, that is also exposed to mechanical failures and needs redundant and heavy flight control systems for safety reasons . It is evident that removing this devices would be translated into a higher fuel capacity, weight reduction and thus an increased range and efficiency.

1.3. Flow control techniques

Potential flow theory is able to describe some fluid mechanics phenomena, but is not accurate enough for cases in which viscosity and boundary layer play an important role, for instance airfoils. Boundary layer theory was firstly introduced by Prandtl in the beginning of the 20th century, being described as a thin layer in which the velocity of the fluid increases from zero at the wall (no slip condition) to its full value corresponding to the external frictionless flow.

Since the introduction of this concept several studies have been done in the direction of separation control through boundary layer manipulation and energizing. It has been proved that that Flow Control techniques achieve drag reduction, lift augmentation, noise mitigation and hereby fuel consumption reduction. Besides the aforementioned advantages the real world applications of this techniques are poor, some reasons to explain that are the inherent complexity of this concept, the amount of energy required for some applications and the conservative point of view of aerospace industry [4].

Flow control techniques are dived into passive and active, that will be further explained in the following sections.

1.3.1. Passive Flow control

Passive flow control techniques deal with flow separation without introducing energy on the system, they are based on mixing high momentum fluid to areas of low momentum, hence to boundary layers which are on the verge of separation. The higher momentum fluid is achieved by introducing physical fixed elements that destabilize the flow in order to obtain a turbulent boundary layer or vortexes transporting a high momentum stream[6].

It has been proved that turbulent boundary layers have an increased momentum in comparison with laminar. In Schlichting's Boundary Layer Theory book we can find this assumption proved: "In a flow at very low Reynolds numbers (laminar flow) [...] viscous forces slow down the particles near the wall in relation to those in the external core. [...] However, observation shows that this orderly pattern of flow ceases to exist at higher Reynolds numbers, and that strong mixing of all the particles occurs. [...] The pattern of streamlines at a fixed point becomes subject to continuous fluctuations and the subsidiary motion causes an exchange of momentum in a transverse direction because each particle substantially retains its forward momentum while mixing is taking place. As a consequence, the velocity distribution over the cross-section is considerably more uniform in turbulent than in laminar flow. " [1]

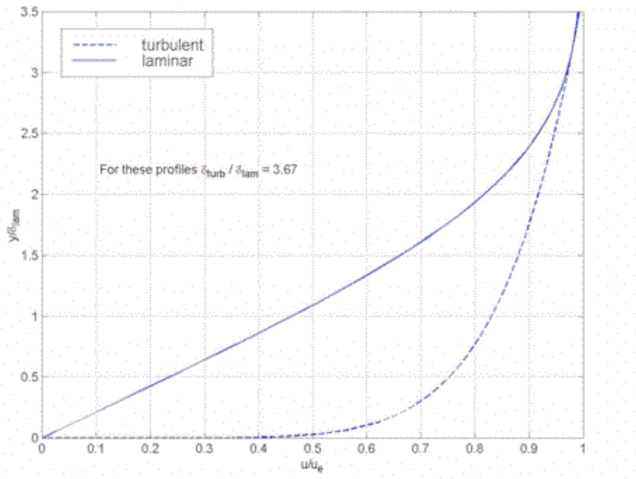

Figure 1.4: Comparison of averaged velocities in laminar and turbulent flow

Comparing time-averaged velocity distributions inside a boundary layer for laminar and turbulent flow over a flat plate (shown in figure 1.4) and taking into account the aforementioned assumptions we can assure the following characteristics for this type flow:

- The flattening of the velocity profile implies an increased velocity near the wall and a better distribution of kinetic energy through the BL, this is translated into a higher momentum.
- The higher velocities near the wall result by definition (1.2 and 1.1) in an increased wall shear stress , and a bigger skin friction drag.

$$C_f = \frac{\tau_w}{1/2\rho u_\infty^2} \tag{1.1}$$

where Cf is the skin friction drag coefficient, ρ is fluid density, u_∞^2 is the free stream velocity, and τ_w is:

$$\tau_w = \mu(\frac{\partial u}{\partial y})_{u=0} \tag{1.2}$$

where μ is kinematic viscosity and $(\frac{\partial u}{\partial y})_{u=0}$ is the wall-normal gradient of streamwise velocity.

- The increased momentum and thus higher kinetic energy near the wall is able to negotiate positive pressure gradients in a better way than laminar would do, for this reason flow separation is delayed or even suppressed.

In today's aviation industry passive flow control devices are used for the aforementioned results that they are able to obtain and for the fact that don't require any power supply to work. However there is an inherent penalty for this type of devices, since they are fixed elements over the aircraft surface they still work when they are not needed, incurring in an unnecessary skin friction drag. Despite this disadvantage, currently we can find Vortex Generators installed over wings and nacelles of the most recent airplanes, such as the Boeing 787 and Airbus A350.

Figure 1.5: Vortex Generators on a Boeing 737-800 wing

Vortex Generators are the most used used passive flow control devices, its functioning its simple but effective. Its geometry is based on a plate forming an angle of attack with the free stream flow, generating this way stream-wise vortexes. With an appropriate dimensioning and positioning, normally previous to separation point, can be used to prevent early flow detachment over the wings, control surfaces and high-lift devices.

1.3.2. Active Flow control

Active flow control techniques are based in introducing high momentum fluid or adding energy to a fluid to modify natural flow characteristics over a certain surface. In comparison with passive techniques they are able to obtain higher improvements in terms of lift enhancement and drag reduction, moreover they can be turned off in situations where they are not needed, for example in cruising flight, not incurring this way in an unnecessary skin-friction drag. [7]

Since the introduction of boundary layer theory in 1904 AFC techniques based in steady suction and blowing have been studied and tested being summarized an reviewed by Lachmann (1961). During this period the only operational use was on military aircraft, but it was disregarded due to the complexity of the plumbing systems and added weight. It was Schubauer and Skramstad (1947) [7] who firstly introduced the concept of unsteady actuation achieving to delay separation with acoustic perturbations, this opened a new range of possibilities showing a much more efficient way to manipulate a flow than conventional steady actuation.

In the recent years progress made with computer capabilities has enabled a growth in this field, since now is possible to use numerical tools for unsteady flow calculations. Several studies have been performed obtaining interesting results, a good example is a NASA/Boeing research [8] to enhance aerodynamic efficiency of a vertical tail. In this research sweeping jet actuators were used to delay flow separation over a highly deflected rudder, increasing the available side force to compensate the rotating momentum generated by a failed engine with a smaller vertical tail.

1.3.2.1. Active Flow control actuation

There are several methods for implementing active control, which can be divided into predetermined or interactive. A predetermined method of control involves the introduction of steady or unsteady energy inputs without consideration for the state of the flow field. In interactive methods the power input to the actuator is continuously adjusted based on measurement elements. The control loop for interactive control can be either a feed forward (open) or feedback (closed) loop.

For both predetermined and interactive methods a wide range of actuators can be employed, they are divided in three main categories depending on their interaction with the outer flow as it is shown in figure 1.6 . Fluidic actuators are the most common, they are based in fluid injection or suction, an example of them are sweeping jets and synthetic jets that will be further explained in the following sections. Moving body actuators interact with the flow using motion of physical surfaces, piezoelectric flaps are an example. Plasma actuators are based in the introduction of electrodes that ionize air, now called plasma. This produces forces due to the attained electric field gradients that can induce velocity components to the flow [7].

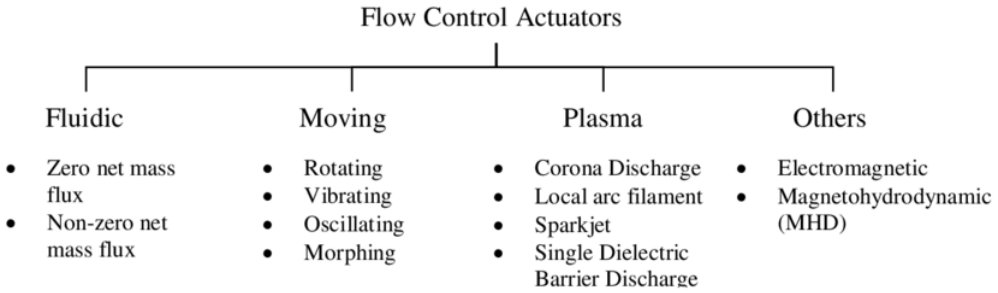

Figure 1.6: Three forms of flow control actuators [19]

1.3.2.2. Sweeping jets

It is called a sweeping jet the outcome of a fluidic oscillator actuator with non-zero net mass flux that produces spanwise oscillating jets, it emits a continuous jet that swings from one side of the outlet nozzle to the other. Such actuators have been found to be more efficient for controlling flow separation in terms of mass flow requirements compared to constant blowing and suction, an example of its effectiveness is the aforementioned Boeing/NASA research that achieved with a momentum coefficient injection of 2% an increased side force in excess of 50%.

The physical functioning of this device achieves self-induced and self-sustained oscillations without moving parts. As it can be shown in figure 1.7 it is composed of 3 main parts, the mixing room, two feedback channels and the nozzle. The pressurized air supplied attaches to either side of the mixing room due to Coanda effect, then pressure increases in the feedback loop and pushes the jet to the other side increasing again the pressure of the other feedback loop. This process is repeated cyclically, the frequency and spanwise sweeping extent depend on the geometric parameters and mass flow rate entering the actuator [11].

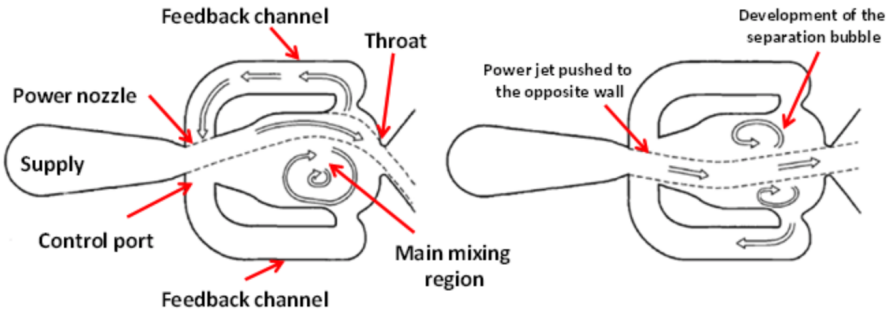

Figure 1.7: Schematic of a conventional curved sweeping jet [11]

1.3.2.3. Synthetic jets

Synthetic jets are zero net mass flux flow control actuators. As it is shown in figure 1.8 this class of actuators are based in an oscillatory surface within a cavity that alternately ingests and expels fluid through a slot, changes in the volume of the cavity are brought about by some mechanism such as a piezoelectric diaphragm or an oscillating piston.

This process often generates vortex rings at the edges of the orifice in a jet-like form, imparting this way finite vorticity into the surrounding fluid. Interaction of these vortices with the surrounding flow enhances mixing with external flow and adds momentum energizing the boundary layer.

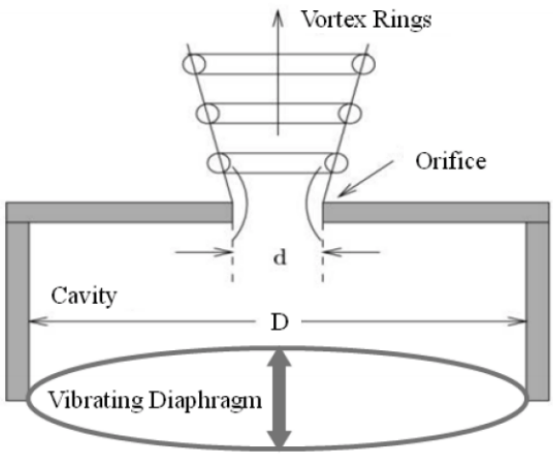

Figure 1.8: Schematic of a Synthetic Jet [20]

The versatility of these actuators is primarily attributed to the following factors:

- The forcing provided by synthetic jets is unsteady and this can be more effective than steady jets.
- Since the jets are synthesized from the working fluid, they eliminate the need for complex fluid circuits and accumulators.
- Amplitude or waveform can usually be tuned to a particular flow configuration.

CHAPTER 2. ASSUMPTIONS OF THE STUDY

In this study we will assess flow behaviour arround a NACA 0012 airfoil at a Reynolds 1000 exposed to an angle of attack of 9^o. Under this conditions the airfoil is expected to be in stall, being the baseline to implement an AFC actuation.

- NACA 0012
- Chord = 1
- AoA = 9^o
- Re = 1000
- U_∞ = 1

Lengths and velocities are non-dimensionalised with the airfoil chord and flight velocity, respectively. The CFD program used to solve navier-stokes equations will take into account the following hypothesis for the calculations:

- Incompressible navier-stokes equations, thus compressibility effects are considered negligible.
- Newtonian Fluid: constant viscosity independently of the shear stress, being the stress tensor a linear function of the velocity gradient.
- Negligible thermal effects.
- No turbulence model is applied.

2.1. Reynolds Number

The Reynolds Number is defined as the dimensionless ratio of the inertial forces (resistant to change or motion) to viscous (heavy and gluey) forces characterizing their importance for a certain flow conditions:

$$Re = \frac{U_\infty \cdot L}{\nu} \tag{2.1}$$

Where U_∞ is the characteristic velocity (flight velocity in our case), L the characteristic length (the chord in our case) and ν the kinetic viscosity.

This parameter also allow us to predict whether a flow is laminar or turbulent. At lower Reynolds numbers viscous forces are dominant and the flow is laminar. Turbulent flow on the contrary occurs with higher Reynolds, where inertial forces dominate considerably, resulting in flow instabilities such as eddies and vortices. The flow may also undergo a transitioning phase whereby the flow exhibits neither completely laminar nor completely turbulent characteristics.

Establishing a concrete value whether a Re is high, low or transitional is complex, since the geometry and the orientation of the object to be studied also are relevant on the flow behaviour. For a laminar plate and a sphere for example the transition number from laminar to turbulent may change in an order of magnitude. For an airfoil a Re number range between 10^4 and 10^5 can be defined as a low-Reynolds-number range while it is considered as high when over 10^6.

2.1.1. Reynolds Number influence in the study

The influence of Re number on airfoils can not be neglected since it has a significant impact on the aerodynamic performance. For lower Reynolds numbers, the viscous forces characterize the flow behaviour over inertial forces, consequently the amount of laminar/turbulent flow over the airfoil surface varies. In figure 2.1 a conventional airfoil exposed at different Reynolds number for a moderate angle of attack is useful to asses its influence [9].

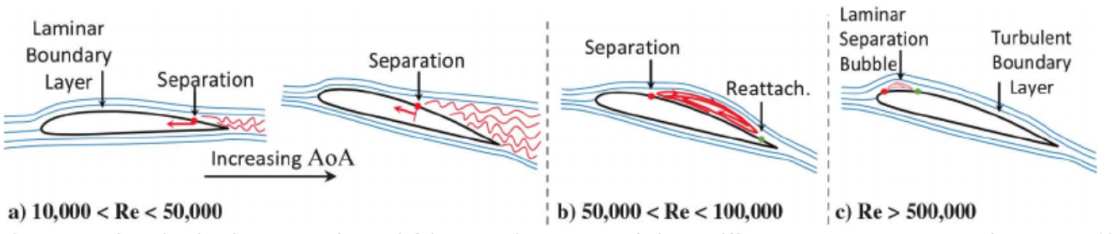

Figure 2.1: Conventional airfoil separation characteristics at different Reynolds number regimes below 10^6

For higher Reynolds (>500,000) in figure 2.1(c) the positive pressure gradient separates the flow near the leading edge, but the shear layer gains momentum from the free-stream and reattaches as a turbulent boundary layer, creating a laminar separation bubble.

Decreasing the Reynolds to 50,000<Re<100,000 results in an increased sized separation bubble as shown in 2.1(b) this behaviour is a consequence of the higher contribution of the viscous forces, resulting in an increased parasitic drag.

At much lower Reynolds numbers 10,000<Re<50,000 (close to our case of study) the separation occurs near the trailing edge for lower angles of attack and as it increases, the separation point moves towards the leading edge. Unlike at higher Reynolds numbers, the shear layer is more resistant to flow transition and is not able to reattach on to the airfoil as a turbulent boundary layer, resulting in high-pressure drag and poor lift generation.

The airfoil used, a NACA 0012, is a widely popular airfoil, which has been experimentally tested for a wide range of Reynolds numbers. It has been proved that reducing Reynolds number affects negatively the airfoil performance as it is shown in figure 2.2. Maximum lift coefficient decreases with Reynolds number and occurs at lower angles of attack, moreover there is an increase of drag coefficient for lower angles of attack. This indicates an early flow separation when Re number is decreased [10].

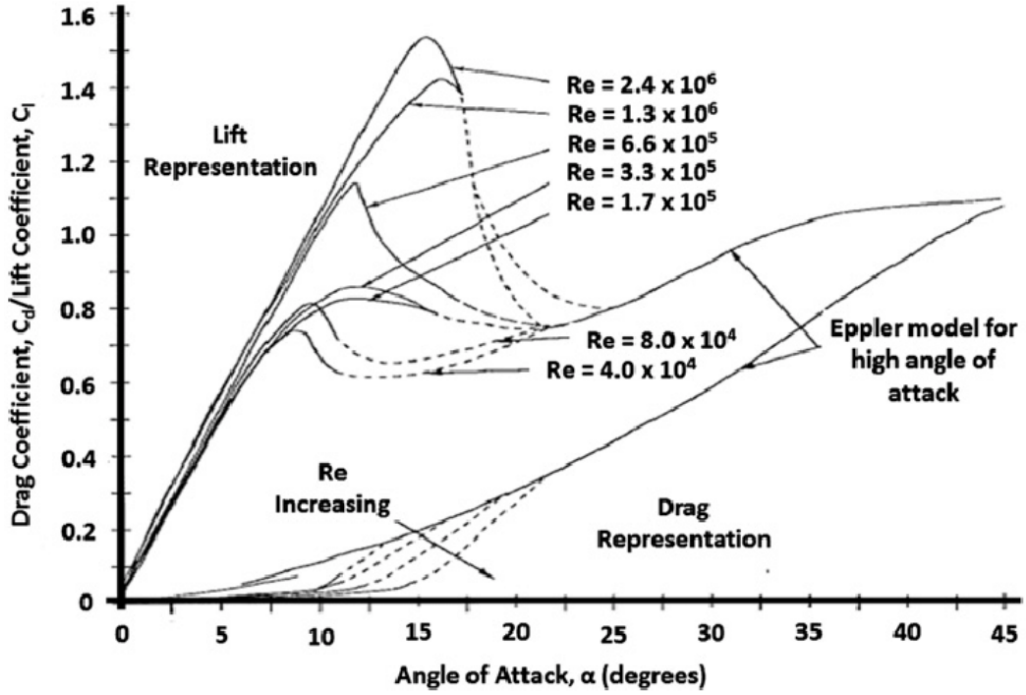

Figure 2.2: Influence of Reynolds number on airfoil NACA-0012 behaviour (Musial and Cromack, 1988)

In our case of study Reynolds number has been set to 1000 being this an ultra low regime. Setting a higher Reynolds would introduce small unsteadiness and perturbations that would only be captured with extremely low time steps and fine meshes. This would be translated into an increased computational power requirement or the introduction of turbulence models, that are currently not available in our CFD solver such as RANS (Reynolds Averaged Navier-Stokes Solver), K-ε, K-ω, SST, etc.

CHAPTER 3. METHODOLOGY

3.1. Simulation Pipeline

In this section the different programs and solvers involved in the resolution of the simulations an its post-processing will be assessed with the objective of having a general point of view of the problem.

When it comes to solving computational fluid dynamics (CFD) problems some procedures have to be followed, in this study it has been done as follows:

1. First step is setting the geometry and the physical bounds of the problem. In our case the coordinates of a NACA 0012 airfoil have been computed using a generic equation for NACA airfoils, once this is done the spacial domain of the problem has been divided into different regions depending on the distance from the airfoil surface. This data is programmed in a script with ".geo" extension that employs GMSH syntax.

2. Second step consists on discretizing the spatial domain previously segregated into finite elements, generating a grid (or mesh). In this study the mesh has been programmed in a structured form using quadrilateral elements. The mesh, also programmed within the previous ".geo" file is saved in a file with ".msh" extension using the open-source mesh-generator GMSH.

3. Next step is converting the previous mesh file into a compatible format for Nektar++, our CFD solver. To do so, a pre-processing routine called *NekMesh* has to be run, its output is an ".xml" file containing the mesh in a suitable format.

4. Fourth step consists on configuring the solver settings, such as the equations to be solved, initial and boundary conditions, variables and other details that would be further explained during following sections. Once this is done the solver can be runned with the command *IncNavierStokes*, having two ".xml" files as inputs containing the mesh and the solver conditions

5. Once the simulation is completed the results are stored in three different file types. The ones with ".chk" and ".fld" extension contain velocity and pressure fields on the full domain, in order to be visualized a change of format has to be done with the command *FieldConvert*, then the results can be displayed using an open-source visualizer called Paraview. The other file remaining, with ".fce"extension, contains the results of a filter previously introduced in in the solver set up, this filter saves the aerodynamic forces over surfaces of interest.

6. Last step is the post-processing of the results, this is done through different Matlab codes. For obtaining lift, drag and its related parameters such as Cl and Cd the results are read from the file with ".fce"extension. On the contrary the data containing pressure coefficient along chord (CP) and wall shear stress (WSS) has firstly to be obtained through Paraview and later being interpreted with a Matlab code.

In the following figure 3.1 a useful schematic summarizing the aftermentioned steps of the simulation pipeline is shown:

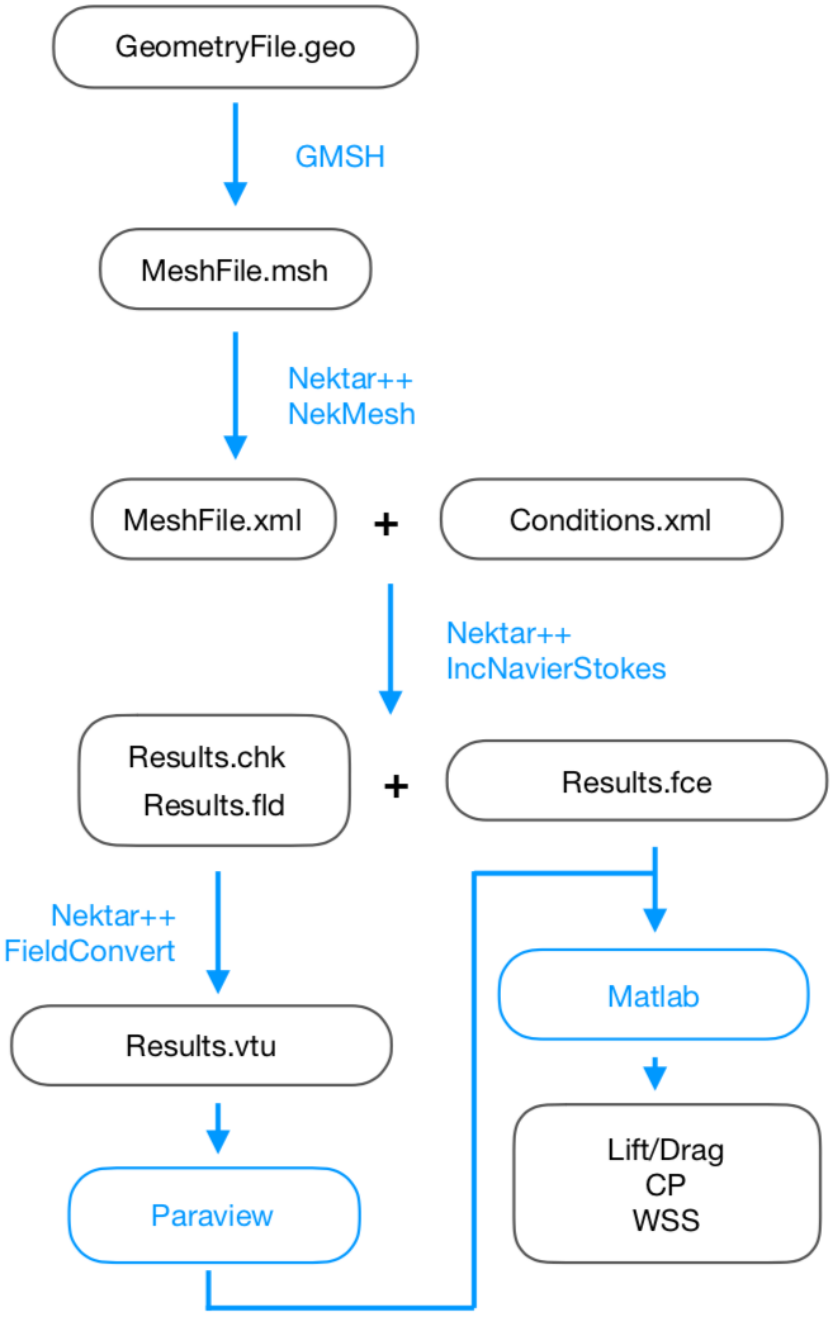

Figure 3.1: Schematic of the simulation pipeline

3.2. Softwares description

3.2.1. Nektar

Nektar++ is a spectral/hp element framework designed to support the construction of efficient high-performance scalable solvers for a wide range of partial differential equations.Software is released as open-source under the MIT license. Although primarily driven by application-based research, it has been designed as a platform to support the development of novel numerical techniques in the area of high-order finite element methods. [14]

3.2.2. GMSH

Gmsh is an open source 3D finite element mesh generator with a built-in CAD engine and post-processor. Its design goal is to provide a fast, light and user-friendly meshing tool with parametric input and advanced visualization capabilities. Gmsh is built around four modules: geometry, mesh, solver and post-processing. The specification of any input to these modules is done either interactively using the graphical user interface, in ASCII text files using Gmsh's own scripting language (.geo files), or using the C++, C, Python or Julia Application Programming Interface (API).[16]

3.2.3. Clufa UPC

The simulations have been carried using this computational cluster. This virtual cluster allows to run multiple tasks (or simulations) at the same time in a constant pace of work. Its technical features consist of:

- Cluster EETAC-HA with 4 servers with a total of 32 cores and 208 Gb of RAM
- Cluster CBL-HA with 3 servers with a total of 44 cores and 224 Gb of RAM

3.2.4. Paraview

ParaView is an open-source software, multi-platform data analysis and visualization application. In this report the figures showing velocity contours and streamlines have been obtained through this software, moreover it was also necessary for the wall shear stress and pressure distribution computations. [18]

3.2.5. Matlab

Matlab is a multi-paradigm numerical computing environment and proprietary programming language developed by MathWorks. MATLAB allows matrix manipulations, plotting of functions and data, implementation of algorithms, creation of user interfaces, and interfacing with programs written in other languages, including C, C++, C, Java, Fortran and Python. [17]

3.3. Mesh

As it has been previously explained, the spacial domain has to be discretized into finite elements where Navier-Stokes equations will be solved. The conjunction of all this finite elements around the airfoil and limited by the boundaries generate the mesh.

In this study a structured 2D c-mesh has been used (shown in figure3.2). This type of grid has been widely employed for CFD analysis of airfoil in viscous flow due to its benefits for modelling wakes after trailing edge. Its main effectiveness lies in its grid configuration, that is stretched in the wall-normal direction of the airfoil while maintains a clustering in the wake region. If an unsteady separation occurs, a process known as vortex shedding, usually leads into the the formation of repeating patterns of swirling vortices, called Kármán vortex street, therefore to correctly model this phenomena is important to have a detailed mesh resolution after the trailing edge.

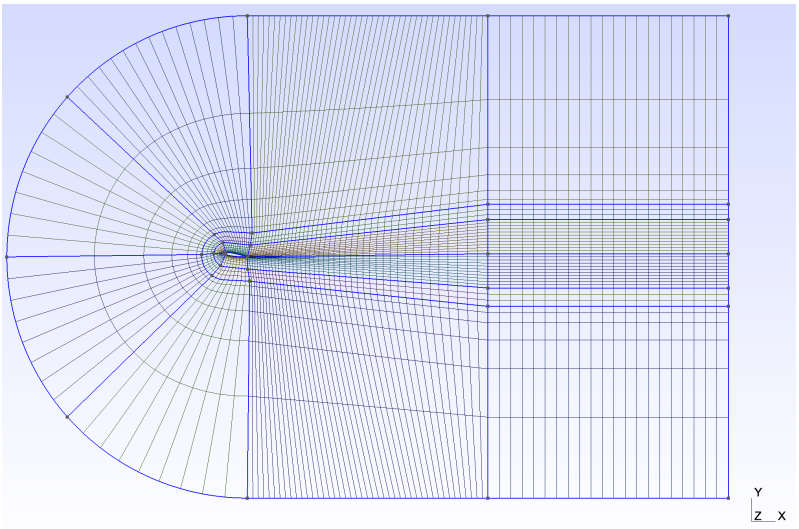

Figure 3.2: Baseline c-mesh

3.3.1. Mesh geometry

The mesh has been configured in such a way that some parameters can be modified and the mesh is capable of automatically adapting to a new geometry and meshing resolution, for instance changes in the angle of attack and the chord.

To do so, in the script file containing the geometry this changing parameters are firstly defined, then the airfoil geometry is introduced with a resolution of 101 points using a NACA MPXX generic equation:

$$y_t = \frac{T}{0.2} \cdot (a_0 x^{0.5} + a_1 x + a_2 x^2 + a_3 x^3 + a_4 x^4) \tag{3.1}$$

Where T is the maximum thickness and for a NACA 0012 the coefficients are: $a_0 = 0.2969$, $a_1 = -0.1260$, $a_2 = -0.3516$, $a_3 = 0.2843$ and $a_4 = -0.1015$ for a blunt trailing edge.

If the airfoil is not cambered (our case) and the chord coincides with the X-axis, y_t is directly the y coordinate of the upper surface of the airfoil and $-y_t$ the lower. For introducing an AoA simply a rotation is introduced.

Once the airfoil is defined, the spacial domain is divided into regions depending on the distance and situation with respect the airfoil. Four main regions can be distinguished:

- Near-field (red)
- Mid-field (orange)
- Far-field (yellow)
- Wake (green)

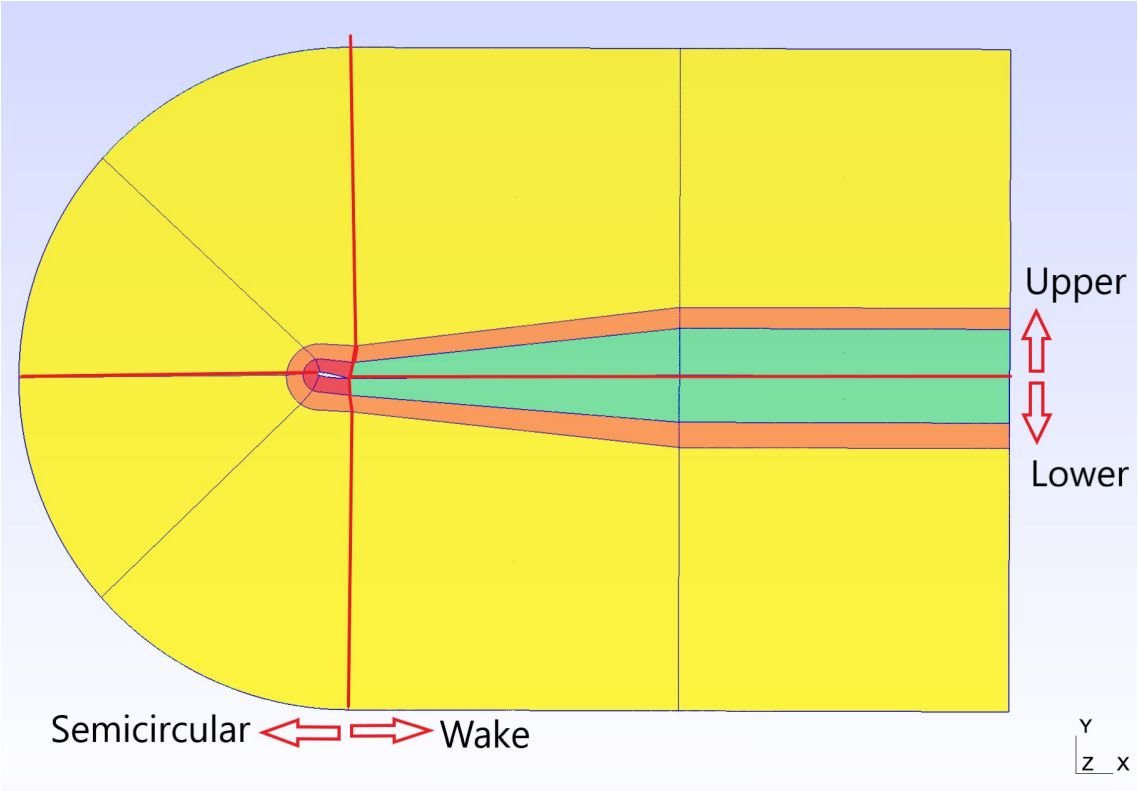

Figure 3.3: Mesh Regions

These regions are defined by the introduction of points and lines using trigonometric equations from the airfoil surface. The extension of the different regions has been delimited as the orthogonal distance from airfoil's surface using the chord as a reference:

- Near-field: 0.5·c
- Mid-field: 1.0·c
- Far-field (upper and lower boundaries): 10·c
- Wake and extended wake: 10·c each (downstream direction)

Having a closer look, in the semicircular region (in figure 3.3) we firstly find a ”c-shaped” line that corresponds to the inlet. As we got closer to the airfoil three regions are crossed; the far-field, mid-field and near-flied where the mesh density is progressively increased. This progression allow us to better define the flow in the airfoil surroundings without introducing excessive cells, improving this way the efficiency of the solver.

After the semicircular region, and passing the airfoil, we can find the wake region, in which the mesh density is progressively reduced from the airfoil trailing edge to the outlet. The importance of this region, as it was previously explained, is to better capture the unsteadiness generated on the airfoil's rear. Extending this section these unsteadiness propagate downstream until their stabilization improving the simulation results.

3.3.2. Mesh discretization

Once the points and lines of the different regions are defined, next step is defining the structured mesh. It is formed by quadrilateral elements, because as the flow orientation can be anticipated they allow a better optimisation of cell count by making them long and aligned with the flow. This is done through the command *Transfinite Line*, in which the number of sub-divisions of the grid in y and x coordinate of a closed region can be defined. Moreover linear progressions can be defined to better detail the mesh in zones where more accuracy is needed. Is the case of the upper surface in the airfoil near-field (shown in figue 3.4), the mesh region with more resolution, where more instabilities are expected to be captured. Is also important to mention, that continuity between all elements in the mesh has to be preserved, this means that the nodes of the boundary of one region must coincide with the adjacent ones.

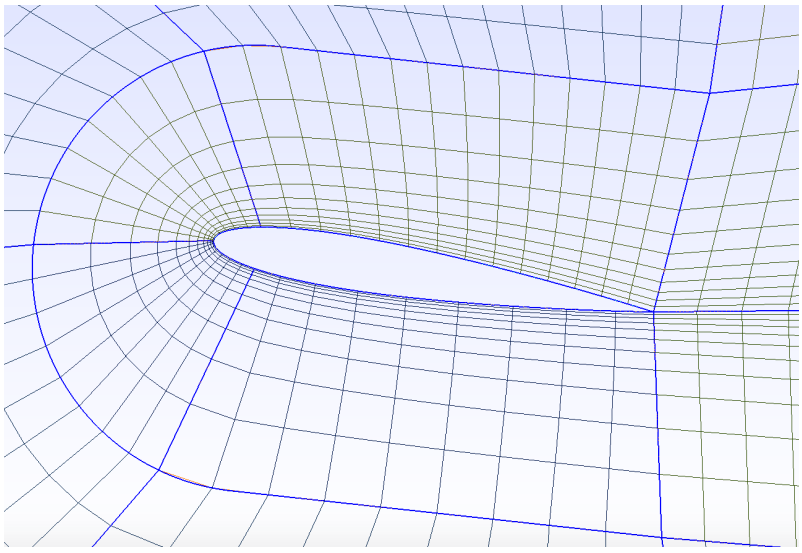

Figure 3.4: Near-field region zoomed

3.4. Navier-Stokes Resolution

Navier-Stokes equations are nothing more than time dependent equations for mass conservation, momentum conservation, and energy conservation equations that govern the movement of a general viscous flow. These equations, firstly derived by G.G. Stokes and M. Navier during the first half of the 19th century, describe how the velocity, pressure, temperature, and density of a moving fluid are related. For an unsteady, compressible and viscous flow the equations for an arbitrary coordinate system are the following:

- Continuity:

$$\frac{\partial \rho}{\partial t} + \nabla \cdot (\rho \cdot \vec{V}) = 0 \tag{3.2}$$

- Momentum conservation:

$$\rho \cdot \vec{g} - \vec{\nabla} p + \vec{\nabla} \tau_{ij} = \rho \frac{d\vec{V}}{dt} \tag{3.3}$$

  Where τ_{ij} is the viscous stress tensor

- Energy conservation: (for a caloricaly perfect fluid $\hat{u}$ = C_v·T and constant coefficients K, μ, C_v).

$$\rho C_v \cdot (\frac{\partial T}{\partial t} + (\vec{V} \cdot \vec{\nabla}) \cdot T) = K \nabla^2 T + \phi \tag{3.4}$$

For a Cartesian reference system in this set of coupled differential equations we will find four independent variables, 3 for the spatial coordinates (x,y,z) and one for the time (t). Moreover we also have six dependent variables; the tree components of the velocity vector (u,v,w), the pressure p, density ρ, and temperature T. All the six dependent variables are function of all the independent variables, therefore we are in front of partial differential equations and not simple ordinary differential equations which are easier to solve. In fact this second-order nonlinear partial differential equations have only a limited number of known analytical solutions, but luckily they are amenable to be solved through discretization and CFD solvers [12].

Nektar++ software has been used for this purpose using its incompressible Navier-Stokes solver for viscous Newtonian fluids, so some hypothesis and simplifications on the general equations will be done:

- Continuty equation:

  Since the fluid is incompressible, the density will not vary neither in time or in the spacial domain.

$$\vec{\nabla} \cdot \vec{V} = 0 \tag{3.5}$$

- Momentum equation:

  The assumption of Newtonian fluid implies that the viscous stresses are proportional to the viscosity coefficient (now assumed constant) and to the element strain rates.

With this assumption the stress tensor can be rewritten in terms of velocity component:

$$\tau_{ij} = \mu \cdot \varepsilon_{ij} = \mu \cdot (\nabla V + \nabla V^T) \tag{3.6}$$

Substituting in the previous equation 3.3 yields to:

$$\rho \frac{d\vec{V}}{dt} = \rho \vec{g} - \vec{\nabla} p + \mu \nabla^2 \vec{V} \tag{3.7}$$

- Energy equation:

  For an incompressible Newtonian flow, where friction does not introduce thermal effects and thus there are no thermal gradients, the equation of energy is not involved in the physics of the problem.

Nektar++ will solve the equation system formed by 3.5 and 3.7 with the further simplification of 2D flow. Now with this simplifications we have three unknowns; the two velocity components *(u,v)* and the pressure *p*. Combining the two equations from the momentum balance and the remaining from the mass conservation results in three equations, so the system is closed and only boundary conditions have to be added.

3.4.1. Spectral/hp element method

Nektar++ solver applies a spectral/hp element method combining this way the geometric flexibility of classical hp-type finite element techniques with the desirable resolution properties of spectral discretisations, that are carried within each final element. Thus this combination tries to bring together the best of both worlds.

The mathematical details for this resolution method are fairly explained in Nektar's user guide [14], so only a briefly conceptual explanation for both methods will be highlighted.

3.4.1.1. hp-element method

This method consists in an improved classical finite element method (FEM). In FEM method the solution is expanded between the nodes of the mesh in a series of linear basis functions, whereas in h-type and p-type the solution is obtained by employing polynomial expansions.

The difference between h-type and p-type FEM methods lies in their different ways to enhance accuracy, in the first one is done by means of a mesh refinement, that is, a reduction in h, while in p-type is achieved increasing the polynomial degree per element. So in hp-version both ideas of mesh refinement and degree enhancement are combined [14].

3.4.1.2. Spectral methods

As opposed to the finite element methods which builds a solution from a sequence of local elemental approximations, spectral methods approximate the solution by a truncated series of global basis functions. Modern spectral methods, involve the expansion of the solution into high-order orthogonal expansion, typically by employing Fourier, Chebyshev or Legendre series [14].

3.5. Solver configuration

In order to set up a simulation two XML files with the geometry and the solver conditions are required. These files contain a number of other sections that describe the configuration for different aspects of the simulation. These sections are the following:

- Geometry:

  The entities composing the mesh, it specifies a list of vertices and edges and how they connect to create the elemental decomposition of the domain.

  - Vertex, Edge, Element, Curved.
  - Composites: Is a list of physical entities in which we will describe the polynomial expansions and impose boundary conditions.

- Conditions:

  Parameters and boundary conditions which define the nature of the problem.

  - Expansions
  - Solver information
  - Parameters
  - Boundary conditions
  - Filters

3.5.1. Expansions

This section specifies the order of the Legendre polynomial expansions to be applied on each element of the defined geometric composites. This composites are closed regions of the mesh, so different expansions are applied keeping in mind the distance to the airfoil surface. It has been done as follows:

- Far-field: 4th order
- Mid-field: 6th order
- Near-field and wake: 8th order

3.5.2. Solver information

It specifies the equations to solve, the solver type, the method of time integration and other parameters that define the actions for the solver. In this case we specify *"UnsteadyNavier-Stokes"* as the equations to solve, and the solver type is *"VelocityCorrectionScheme"*.

The Velocity Correction Scheme uses splitting/projection method to solve Navier-Stokes equations where the velocity and the pressure are decoupled. In brief, the velocity is firstly obtained without considering the pressure, then the pressure field is solved and a correction is applied to the velocity. This method may induce some error when the

velocity and the pressure are decoupled, but if it is done consistently it helps to improve the numerical efficiency. The time stepper used is second order implicit-explicit, also other options have been selected they are shown in 3.5.

```
<CONDITIONS>
  <SOLVERINFO>
    <I PROPERTY="SOLVERTYPE"              VALUE="VelocityCorrectionScheme"  />
    <I PROPERTY="EQTYPE"                  VALUE="UnsteadyNavierStokes"    />
    <I PROPERTY="Projection"              VALUE="Continuous"              />
    <I PROPERTY="EvolutionOperator"       VALUE="Nonlinear"               />
    <I PROPERTY="TimeIntegrationMethod"   VALUE="IMEXOrder2"              />
    <I PROPERTY="Driver"                  VALUE="Standard"                />
    <I PROPERTY="AdvectionForm"           VALUE="SkewSymmetric"           />
    <I PROPERTY="Extrapolation"           VALUE="Standard"                />
  </SOLVERINFO>
```

Figure 3.5: Solver Information for unsteady incompressible Navier-Stokes resolution

3.5.3. Parameters

In this sections all the parameters needed for the solver and used along the code are defined. For the time integration method some paremeters must be defined, being ”TimeStep” and ”NumSteps” are the most significant. The ”TimeStep” has to be fixed small enough that enables capturing the unsteadiness of the flow, but also taking into account that it affects the total time simulation. The ”NumSteps” have to be adjusted bearing in mind the time required to obtain a converged simulation. For a standard simulation the following parameters have been set:

- TimeStep = 0.0001
- NumSteps = 500000

3.5.4. Boundary conditions

Three types of boundary conditions are used, Dirichlet, Neumann and Robin conditions. Dirichlet condition consists in specifying the value of the solution along the boundary region, this is denoted in the code with the letter ”D”. Neumann, denoted with ”N”, specifies the value in which the gradient normal to the boundary is applied. For the Robin condition a relation between the value and the gradient of the variables is imposed.

For the different boundary regions, the conditions are applied as follows:

- Inlet

  In this section the value for the U_∞, the free stream velocity, is defined imposing a Dirichlet condition to the ”u” velocity component of value 1, the normal component ”v” is fixed to 0. For the pressure the Nektar’s recommended condition has been used, in which a high-order (denoted with ’H’) Neumann boundary condition with 0 initial value has been set.

- Upper and lower boundaries

  In this region gradient of u normal to the boundaries is set to zero through a Neumman condition. Indicating that there is no mass flux getting out of the control volume through these boundaries and that the boundary is far enough from the airfoil that can be considered free stream. It is a slip wall boundary condition.

- Airfoil surface

  Since our fluids is viscous no-slip wall condition has to be applied over this surface, so the velocity over this surface has to be strictly 0 as much for the ”u” and ”v” velocity components. This is set through a Dirichlet condition.

- Outlet

  Energetic vortices are expected to cross the outlet region, so a special treatment has to be carried over this region in order to avoid instabilities. Nektar suggests using a convective like outflow condition using a USERDEFINEDTYPE “HOutflow” as shown in 3.6

```
<REGION REF="1">
  <R VAR="u" USERDEFINEDTYPE="HOutflow" VALUE="0" PRIMCOEFF="D0/TimeStep" />
  <R VAR="v" USERDEFINEDTYPE="HOutflow" VALUE="0" PRIMCOEFF="D0/TimeStep" />
  <R VAR="p" USERDEFINEDTYPE="HOutflow" VALUE="0" PRIMCOEFF="1.0/(D0*Kinvis)" />
</REGION>
```

Figure 3.6: Outlet Boundary conditions

3.5.5. Filters

The filter ”AeroForces” has been added, this filter evaluates the aerodynamic forces along a specific surface, in our case the closed region that defines the airfoil. The forces are projected along the Cartesian axes and the pressure and viscous contributions from both lift and drag are computed in each direction. The output of this filter is stored every ten time steps in a file with ”.fce” extension.

3.6. Convergence study

In the previous study the accuracy degree of the results was studied by performing different simulations modifying the elements that fundamentally affect the precision of the results with the objective of finding a trade-off between precision and the time required per simulation. The main aspects that directly deal with the precision of the results are; the control volume sizing, the mesh resolution control through the expansions and the time step between iterations.

In this section we will compare the accuracy of the results with the variables chosen in the previous study with the aim of determining its reliability and the significant digits that will be taken into account in the simulations. The comparison will be made through a simulation with an increased mesh resolution and also with a external CFD solver, XFOIL.

The choosen parameters for the control volume expressed in therms of the chord length are the following (in table 3.1):

Mesh Region	Size
Semicircular Region radius	10·c
Wake	10·c
Extended wake	10·c

Table 3.1: Control Volume sizing

The baseline expansions over the different composites or physical surfaces composing the spacial domain are represented in the following table 3.2:

Physical Surface	Abbreviation	Polynomial Expansions
Far-Field	FF	4
Upper-Mid Field Wake	UMFW	6
Mid-Field Except Upper-Wake	MFEUW	6
Upper-Near Field	UNF	8
Lowe-Near Field	LNF	8
Wake	W	8

Table 3.2: Expansions over the different composites

For the comparison using the same CFD solver, Nektar++, the mesh sizing has been maintained and the polynomial expansions have been increased, expecting this way an improved results. The time step has been also kept constant. The values for comparing the precision will be the lift and drag coefficients, and are summarized in the following table 3.3:

FF	UMFW	MFEUW	UNF	LNF	W	TimeStep	Cl Mean	ε_{Cl} %	Cd Mean	ε_{Cd} %
4	6	6	8	8	8	0.0001	0.37509	0.01	0.15265	0.01
5	7	7	9	9	8	0.0001	0.37514	0	0.15267	0

Table 3.3: Accuracy comparison with Nektar++

The comparison with another solver isn't necessary to asses the accuracy unless we know with certainty that the other solver is more precise, but it is useful to crosscheck our results with different sources to realize that we are not incurring into a systematical error.

XFOIL is an interactive program for the design and analysis of subsonic isolated airfoils developed by Mark Drela at MIT Aero & Astro [13]. In between its functions it allows to predict pressure distributions and hence lift and drag coefficients for airfoils in viscous flow conditions allowing the following cases:

- Forced or free transition.
- Transitional separation bubble(s).
- Limited trailing edge separation.
- Lift and drag predictions just beyond CLmax.

Our case of study is a trailing edge separation before CLmax, so this solver should be capable of computing reliable results. The results obtained are quite similar to the ones obtained by Nektar++ as it can be shown in the figure 3.7, where a pressure coefficient plot is represented comparing the inviscid limit (white) with our solution (blue and red).

The lift coefficient has an error of 0.25% compared with Nektar solution and for the drag coefficient the error is 0.58%. As a conclusion and taking into account all the obtained results the Nektar solution will be considered accurate with 4 significant digits.

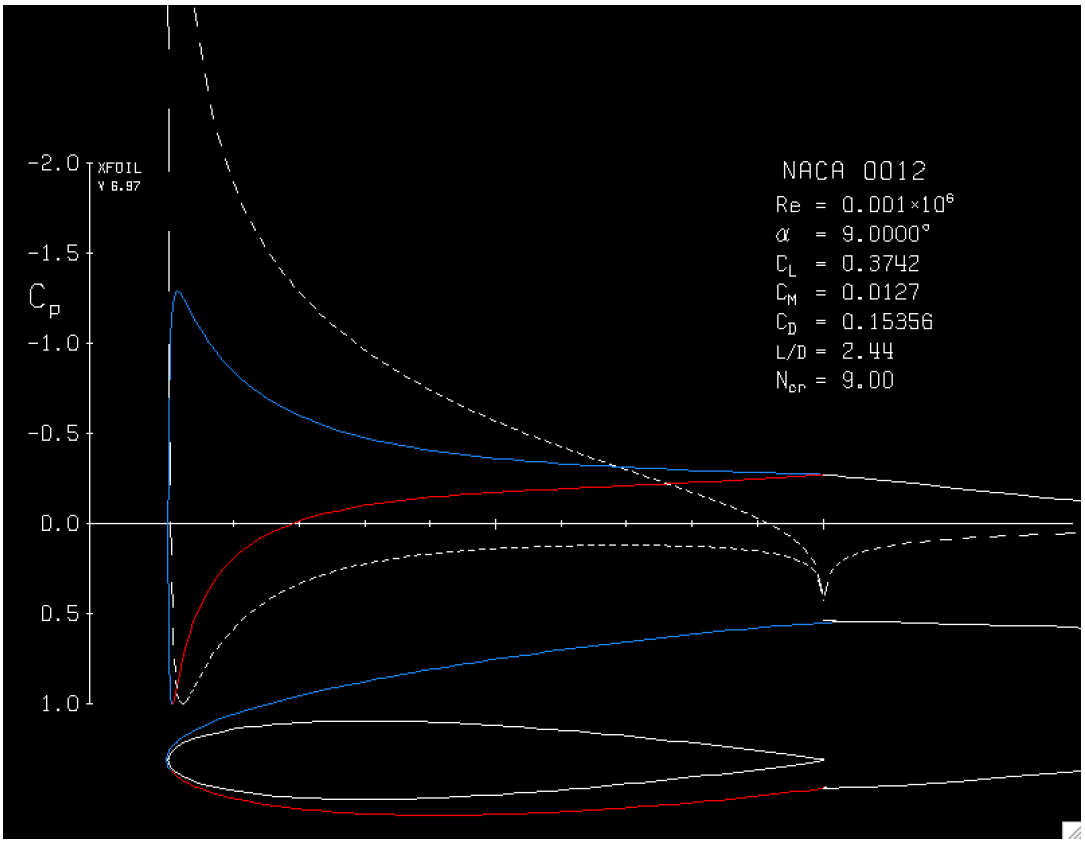

Figure 3.7: Xfoil results

CHAPTER 4. BASELINE RESULTS

4.1. Flow natural behaviour

In this study we start from a previous research [15] where a sweeping jet actuation was successfully proved for improving airfoil performances at ultra-low Reynolds. These results provide us the baseline to continue the research, but firstly is necessary to analyze the natural flow behaviour to better understand what we are dealing with. To do so, a simulation will be carried and some key parameters will be analyzed to finally obtain the baseline airfoil performances.

The simulation parameters are the same than in the assumptions section, Re=1000, AoA=9^o and moreover a standard jet slot that will be used during the simulations has been also included over the airfoil geometry located at 73% of the chord, this slightly modified geometry and remeshing are explained in section 5.1..

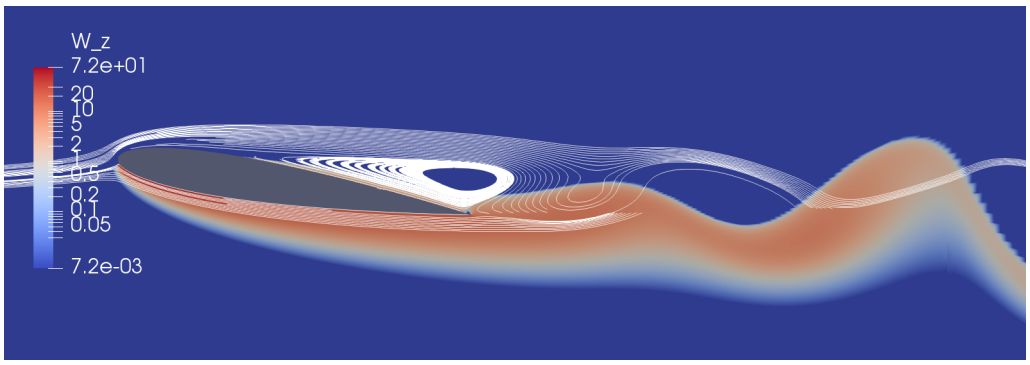

Figure 4.1: Baseline vorticity contour and streamlines

With the vorticity contour shown in the figure 4.1 we can clearly realize that we are in front of a trailing edge separation that is fairly extended towards the leading edge. Considering the streamlines is also evident that this solution is not stationary since there is a presence of periodic vortex structures, this phenomena is known Karman vortex street. Having a closer look into the trailing edge is noticeable the presence of a trailing edge vortex.

4.1.1. Baseline airfoil performance

By definition the boundary layer detachment occurs when the shear stress τ_w is canceled or equal to 0. To find out the position where it takes place the WSS (wall shear stress) has been extracted from the solution and has been plotted over the normalized chord ς/c. The two instants corresponding to the maximum an minimum lift coefficients have been represented in order to show that the separation point remains pretty much constant. In figure 4.2 three peaks can be clearly distinguished, the first one corresponds to the boundary layer detachment and it occurs about 34% of the chord, whereas the second one is artificially induced due to the presence of a jet slot over the upper surface, finally the last one, almost at the end of the trailing edge at 97% of the chord confirms the presence of a trailing edge vortex.

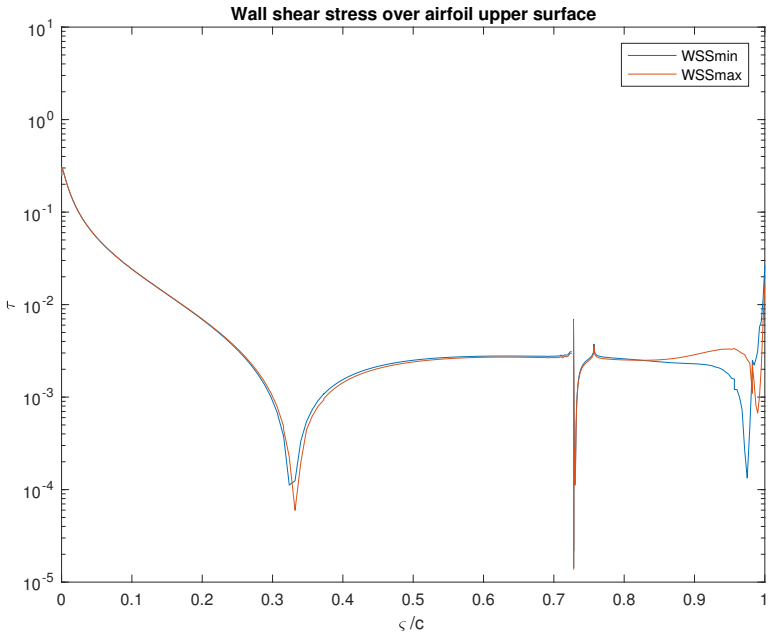

Figure 4.2: Baseline wall shear stress for the maximum and minimum lift coefficient instants.

The unsteady solution obtained due to the vortex shedding is also translated into an unsteady oscillating lift and drag response (as shown in figure 4.3). To obtain its mean values a Fourier transform has been applied to each signals using the Matlab function *fft* (Fast Fourier Transform) and disregarding the transient response to obtain more accurate results, it is considered that the stabilization takes about 30 seconds. From this operation also the main vortex shedding frequency f_0 is obtained with a value of 0,892Hz corresponding to the first peak of the Fourier transform.

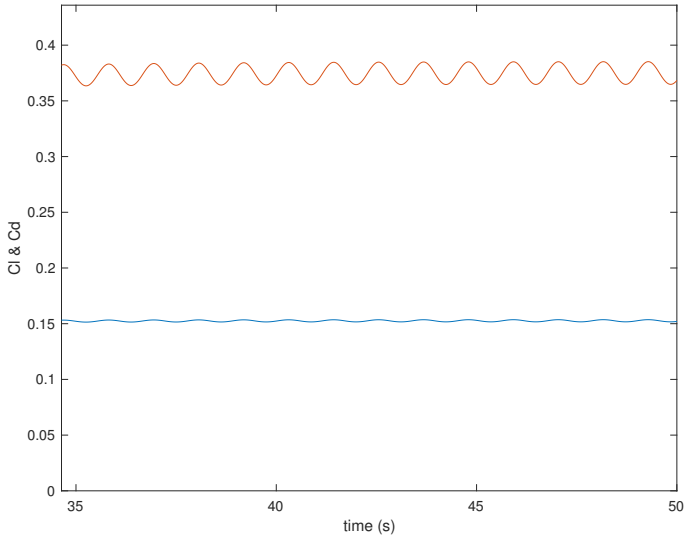

Figure 4.3: Baseline lift and drag coefficients time response

To compute lift and drag coefficients a Matlab script has been used to read a Nektar file containing the aerodynamic forces over the surfaces of the airfoil. Since the density, the velocity and the chord are set to 1 the coefficients are simply:

$$Cl = \frac{2 \cdot L}{\rho \cdot c \cdot U_\infty^2} = 2 \cdot L \tag{4.1}$$

$$Cd = \frac{2 \cdot D}{\rho \cdot c \cdot U_\infty^2} = 2 \cdot D \tag{4.2}$$

In this script in addition to the total lift and drag forces there is also data from the viscous and pressure drag components that will be useful to assess the influence of the implemented actuation on these parameters, a summary of the main characteristics is detailed in the table below 4.1:

Cl	0.3748
Cd	0.1527
Cd_v	0.0754
Cd_p	0.0773
L/D	2.454
f_0	0.892

Table 4.1: Baseline results

4.2. Baseline Actuation

In the previous research [15] an AFC actuation was tested with the aim of improving the baseline performance of the NACA 0012 airfoil at 9^o of AoA. The actuation tested was based in the use of Sweeping jets in two configurations, injecting fluid in the streamwise and in the streamwise-normal direction. In this section their best results are presented and the aspects that can be improved have been highlighted.

4.2.1. Streamwise-normal sweeping jet

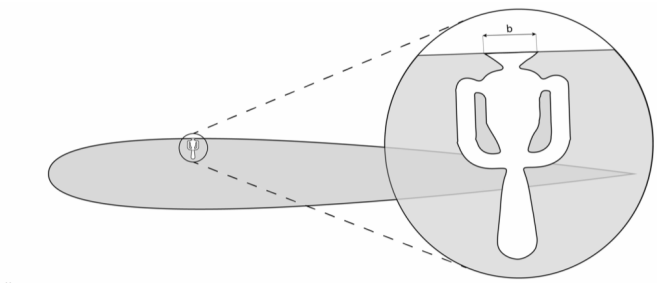

Figure 4.4: Streamwise-normal sweeping jet [15]

In this actuation the device cavity was not included in the airfoil geometry, instead a boundary condition in a certain region over the upper surface was applied to inject fluid in normal

direction to the airfoil on the jet's position, as it is shown in figure 4.4. The chosen variables to control the jet actuation were the positioning over the surface expressed in terms of chord percentage, the momentum coefficient that quantifies the quantity of fluid injected and its velocity and the frequency of oscillation expressed in terms of the baseline vortex shedding frequency "fo".

The results obtained with this actuation were poor or even aggravated the baseline performance. In the table 4.3 a summary of the best results with its jet parameters (momentum coefficient, oscillation frequency and jet position) is shown.

Jet Position	C_μ	Jet Frequency	Cl	Cd
Baseline	-	-	0.3748	0.1527
34%	0.12%	fo	0.3604	0.1584
70%	0.12%	$2 \cdot fo$	0.3559	0.1513

Table 4.2: Streamwise-normal Sweeping jet best results and baseline comparison

4.2.2. Streamwise Sweeping Jet

In this actuation, however, the jet was included in the airfoil geometry with a step shape (as shown in figure 4.5), its size was established as a 0.3% of the chord. The main difference remains in its orientation, that now is quasi-tangential to the airfoil surface.

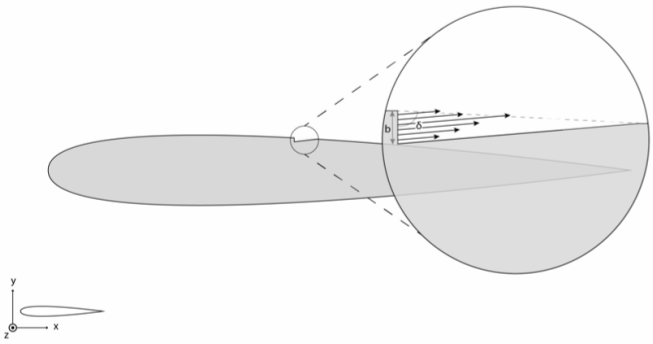

Figure 4.5: Streamwise sweeping jet [15]

The fluid injection was introduced also through a boundary condition and two cases were studied. The first one was a constant momentum injection, or in other words a steady jet. The second one was an oscillating jet that varied its mass flux in the same tangential direction of the fluid injection. The frequency of the oscillation was also expressed in terms of the vortex shedding frequency "fo" and the jet's output velocity u_j for this case is defined as the addition of a constant velocity u_0 plus an amplitude term $a \cdot u_0 \cdot cos(\omega t)$.

The variables to test the effectiveness of this actuation were the jet position over the airfoil surface, the amplitude of the oscillation and its frequency. Firstly a jet position that maximizes the overall performance was tried to be found out, considering that the jet was unable to completely reattach the boundary layer but was able to increase the suction before its location the jet was moved towards the trailing edge, precisely its best position was found to be at 73% of the chord.

In relation to the amplitude and frequency impact on the airfoil performance several simulations were carried increasing the amplitude and the frequency of oscillation. The result of modifying these variables induced several downsides. As the amplitude was increased the lift coefficient decreased and the drag coefficient followed suit, but the overall efficiency (lift to drag ratio) decreased. The effect of increasing the frequency exceeding the vortex shedding induced huge oscillations on the lift temporal signal without introducing any other benefit.

In conclusion the best results for this actuation were obtained at a jet position of 73% of the chord with a constant-net mass flux sweeping jet, they are summarized in the following table 4.3:

C_μ	7%
Jet width	0.3%·c
Jet position	73% ·c
Jet frequency	0
Cl	0.5469
Improvement %	45.9%
Cd	0.2112
Improvement %	-38.3%
L/D	2,59

Table 4.3: Streamwise sweeping jet best results summary

CHAPTER 5. SIMULATION RESULTS

The streamwise sweeping jet configuration was found to be effective in improving the airfoil performance, an increase of nearly 46% of the lift coefficient was achieved but the drag coefficient suffered a deterioration of almost a 40%. This worsening is owing to the viscous drag term, that had been increased due to the high velocities generated by the sweeping jet near the surface, on the contrary the pressure drag was reduced by approximately a 50% by the postponement of the boundary layer detachment [15].

In this study the simulations are on the way of mitigating the drag coefficient penalty while maintaining or increasing the lift improvement. Some hypothesis have been done and the following parameters will be changed:

- **Jet width:**

  Increasing the jet width while maintaining the same momentum coefficient will decrease the jet's output velocity and this way the viscous drag term should be reduced.

- **Jet angle:**

  The streamwise or tangential injection of fluid was shown to be more effective than in a normal direction to the airfoil surface, but injecting fluid in an angle in between those studied cases should also reduce the viscous drag term, because of the distancing of the high velocities of the jet with respect the airfoil surface.

In addition to this changes different jet configurations will be studied:

- Blowing jet
- Suctioning Jet
- Synthetic Jet

5.1. Mesh adaptation

In order to be able to change the aftermentioned parameters of jet width and jet angle the points forming the current jet slot have been redefined.

The wall of the jet cavity in which the fluid is injected is now capable of modifying its angle with respect the chord line as it is shown in figure 5.1, being 90^o of jet angle (γ) a perpendicular wall with respect the chord, thus the angle of injection of the fluid can be modified. In order to not influence the fluid coming out from the jet cavity a perpendicular line has been added from the bottom of the wall until the intersection with the airfoil surface. The fluid injection is made through a boundary condition always normal to the jet wall.

The jet width "b" is expressed in terms of the chord size, initially it was fixed to a 0,3% of the chord but different sizes will be tested during the simulations.

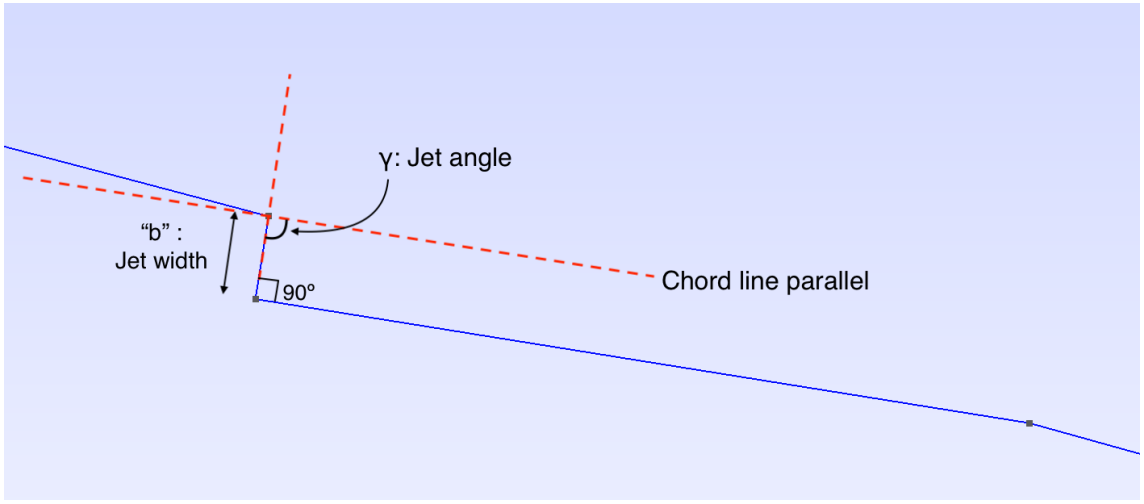

Figure 5.1: Jet slot geometry for a jet angle of 90^o

The quadrilateral surface added in the previous research that is extended along the airfoil surface until the trailing edge has been maintained for the same reason, to satisfy the transfinite algorithm and the mesh continuity, since in this kind of structured mesh the mesh elements can not be triangles, must be quadrilaterals. The mesh resolution in the first quadrilateral, corresponding to the jet slot has been meshed with a higher resolution, since the geometrical changes induced convergence errors. Now the number of horizontal and vertical transfinite lines is 4 and 6 respectively as it can be seen in figure 5.2.

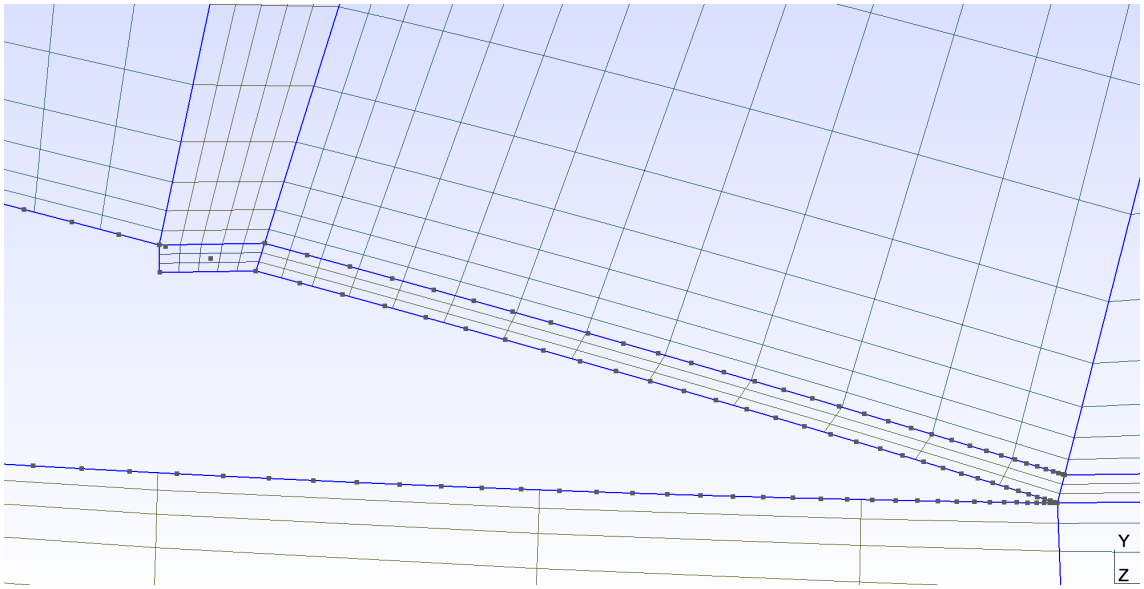

Figure 5.2: Mesh adaptation for the new actuation

5.2. Jet Parametrisation

Before getting down to business is important to define a key parameter involved in all AFC actuations, the momentum coefficient C_μ. With this parameter the fluid injection can be

quantified in relation with the stream flow around the airfoil. In the following sections 5.3. and 5.4. the momentum coefficient is defined as:

$$C_\mu = \frac{\dot{m}_j \bar{u}_j}{\frac{1}{2}\rho_\infty U_\infty^2 c} = \frac{\rho_j \bar{u}_j^2 b}{\frac{1}{2}\rho_\infty U_\infty^2 c} \tag{5.1}$$

Where $\bar{u}_j$ is the mean jet velocity (mass flow divided by jet width), b is the jet width and assuming incompressibility ρ_∞=ρ_j leads to:

$$\bar{u}_j = \sqrt{\frac{C_\mu U_\infty^2 c}{2b}} \tag{5.2}$$

In a real actuation the fluid injection would be done through a pipe, in order to model the fluid coming out of the jet nozzle taking into account the non-slip condition a parabolic velocity profile has been assumed. This is done using a unitary parabola and the jet maximum velocity u_{Jmax}:

$$u_j(x) = (Ax^2 + Bx + C) \cdot u_{Jmax} \tag{5.3}$$

In order to relate the jet maximum velocity with the momentum coefficient the following integral has been performed:

$$\bar{u}_j = \frac{1}{b}\int_0^b u_j(x)dx$$

that for a general unitary parabola leads to:

$$u_{Jmax} = \frac{3}{2}\bar{u}_j \tag{5.4}$$

The three coefficients (A,B,C) of the two degree polynomial *P(x)* that define the parabola are determined setting the following conditions:

$$P(x_0) = 0$$
$$P(x_1) = 0$$
$$P(\frac{x_0 + x_1}{2}) = 1$$

where x_0 and x_1 are the x-coordinates of the top and bottom jet slot. Finally the coefficients are:

$$A = \frac{1}{(\frac{x_0+x_1}{2})^2 + (x_1^2 - x_0^2)\cdot\frac{x_0+x_1}{2\cdot(x_0-x_1)} - x_0\cdot(x_0 + \frac{x_1^2-x_0^2}{x_0-x_1})}$$
$$B = -A\cdot\frac{x_0^2 - x_1^2}{x_0 - x_1}$$
$$C = -A\cdot x_0^2 - B\cdot x_0$$

5.3. Blowing Jet

The actuation in this section will be based on a constant net mass-flux jet, the effectiveness of this configuration in comparison with an oscillating jet has encouraged this decision. The control parameters for this actuation will be the previously described jet width and jet angle and the baseline parameters common for all the simulations are a momentum coefficient Cμ of 7% and the jet located at a 73% of the chord.

- Cμ = 7%
- Jet position: 73% of the chord

5.3.1. Jet width study

The baseline jet width was set in the previous study as a 0,3% of the chord, with the aim of reducing the viscous drag a reduction of the jet output velocity should have a positive impact. As the jet velocity is inversely proportional to the jet width as shown in equation 5.2 the jet width will be progressively increased while maintaining a constant Cμ and keeping the jet angle in a quasi tangential direction (γ=90^o).

The maximum jet output velocities U_{Jmax} for the five jet widths tested, computed with equation 5.2. are shown in the table 5.1. These velocities are in the worst case on the order of five times the stream flow velocity, in a real application compressibility effects should be taken into account, but in this academic research as the Reynolds number is set within an ultra-low regime have not been considered.

Jet width	U$_{Jmax}$
0.3%	5.12
0.5%	3.96
0.8%	3.13
1.0%	2.8
1.2%	2.56

Table 5.1: Maximum jet output velocity U_{Jmax} for every jet width

The jet width impact on the airfoil natural behaviour, what means without introducing a fluid injection ($C_\mu = 0$) has been also studied with the objective of determining the worsening of the airfoil performance that can induce the presence of such an abrupt change of the airfoil geometry.

Jet width	0.3%	0.5%	0.8%	1.0%	1.2%
CL	0.3751	0.3751	0.3748	0.3745	0.3741
CD	0.1527	0.1527	0.1527	0.1527	0.1528

Table 5.2: Jet width influence on the baseline airfoil performance ($C_\mu = 0$)

As it can be seen in table 5.2 the overall performance studied at 9^o AoA, the case of study, is practically not affected by the jet width increase. This behaviour is due to the fact that at

this AoA the jet slot is located after the boundary layer detachment, if the AoA was reduced the effects increasing the jet slot would be with certainty more noteworthy, but in this study this situation will not be considered.

The results for the lift and drag coefficients while introducing a 7% of momentum coefficient and increasing the jet width are shown in the following figures (5.3 and 5.4). The first overall results show benefits for both lift and drag and moreover the solution for all cases is stationary and the vortex shedding has been suppressed.

- The lift coefficient is nearly increased a 7.2% when the jet width is increased from a 0.3% to a 1% from that point on, the lift coefficient starts to decrease.

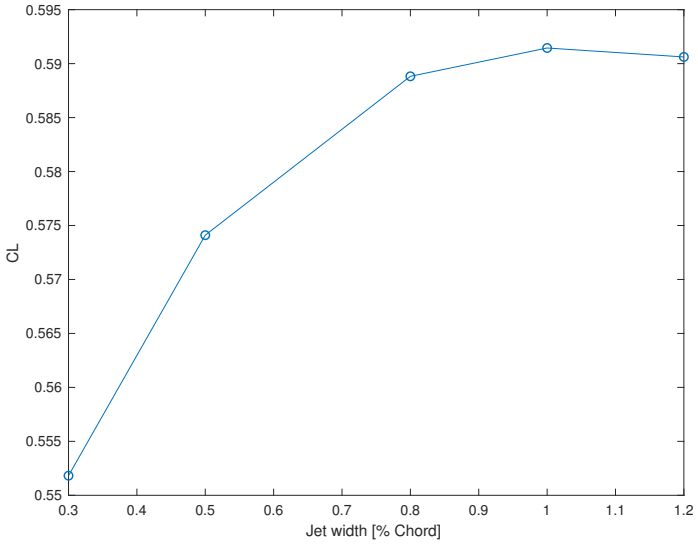

Figure 5.3: CL vs Jet width

- The drag coefficient is also slightly reduced almost a 7.3% when the jet width is increased to the maximum value tested, a 1.2% of the chord.

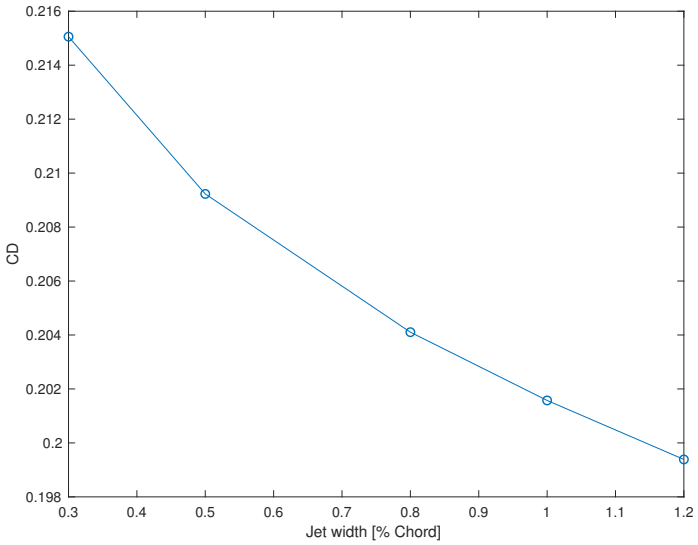

Figure 5.4: CD vs Jet width

Having a closer look to both figures is noticeable that there is a bigger improve for both lift and drag for the first 0.3% to 0.8%, if the jet width is further increased the benefits become less evident or even get worse in the case of the lift coefficient. This behaviour confirms the relation of this improvements with the jet output velocity, since for the range of 0.3% to 0.8% the jet velocity suffers a bigger decrease.

To better explain the improvements of this actuation the viscous and pressure drag coefficients will be analyzed. In the case of viscous drag a reduction while the jet width is increased is expected, and could explain the overall drag reduction.

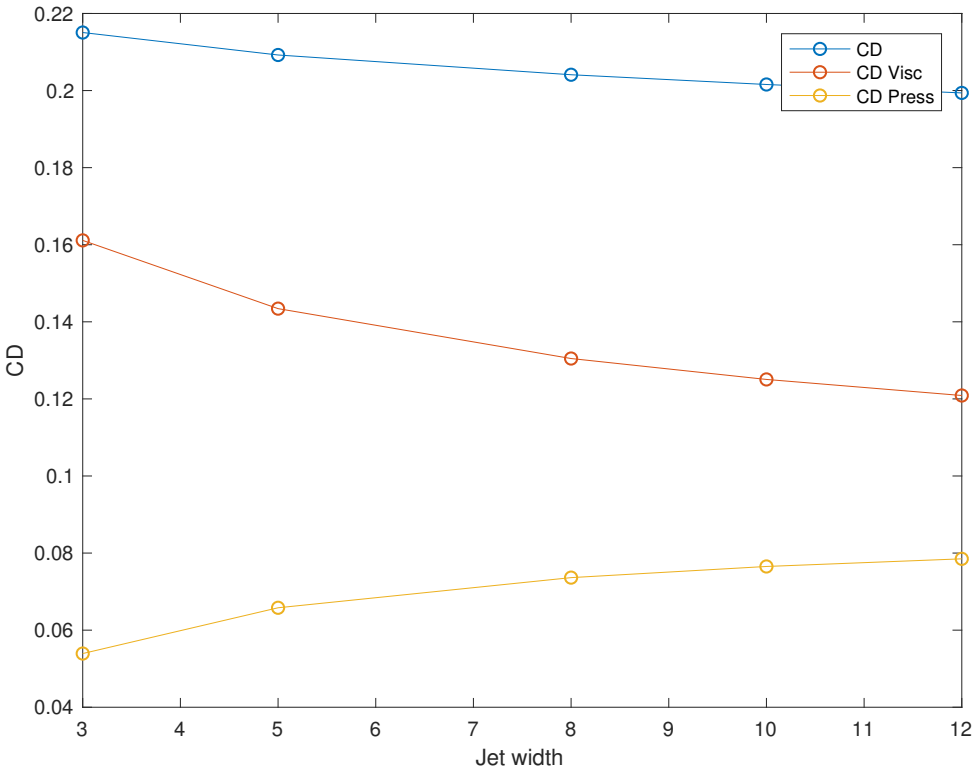

Figure 5.5: Viscous and Pressure drag coefficient vs Jet width

As expected, the viscous drag suffers a reduction of almost a 25% with respect the initial case. Comparing the overall drag reduction with the viscous drag plot in figure 5.5 it can be observed that the reduction is produced in a similar way, but the huge reduction of the viscous drag is not directly translated to the overall drag coefficient, this is due to effect of the pressure drag.

The pressure drag grows in the same way that the viscous drag reduces, but fortunately the overall balance is positive. This effect is probably caused because as the jet width is increased the pressure after the jet region is reduced. To better assess this effect a vorticity contour with its streamlines will be analyzed.

5.3.1.1. *Vorticity and streamlines analysis*

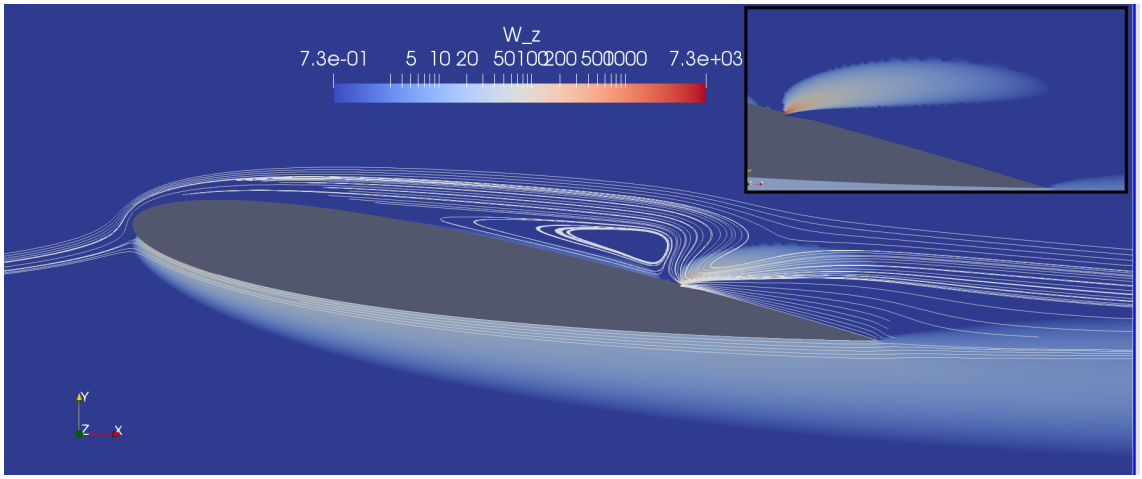

(a) Jet width 0.3%

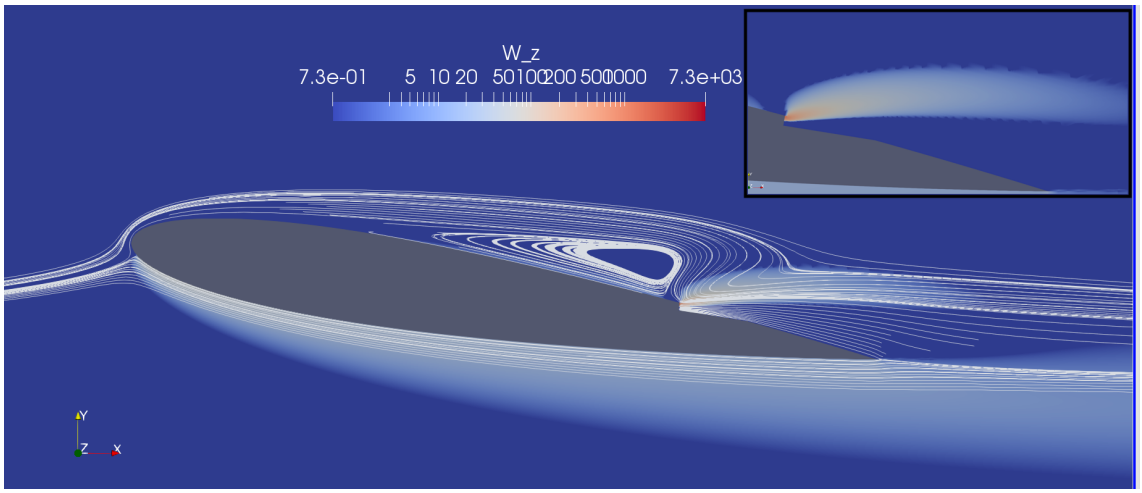

(b) Jet width 1%

Figure 5.6: Vorticity contour and streamlines for jet width 0.3% and 1% actuation

Looking at the two extreme cases in figure 5.6 it can be clearly seen that the baseline oscillating behaviour with a vortex street has been improved to a stationary response. A separation bubble of similar characteristics is formed before the jet for both actuation and just before it a reattachment takes place. This reattachment is maintained until the trailing edge, being the wake now much more stable and clean. The differences between contours with different jet widths are hardly noticeable, but zooming in the jet area (as shown in the insets of the figure 5.6) we can realize that the instability effect range of the wider jet in the flow direction is larger than in the narrower one, so the narrowest jet suffers a higher 'diffusion' than the widest losing momentum and velocity faster. In addition the wake is slightly smother and clean in the wider one.

In the search for more evidences capable of explaining the improvement of lift and drag is also necessary a wall shear-stress plot over the upper surface to analyze the behaviour of flow after the jet and also a pressure coefficient plot to see how the pressure distribution has changed after the actuation.

5.3.1.2. Wall shear stress and pressure distribution analysis

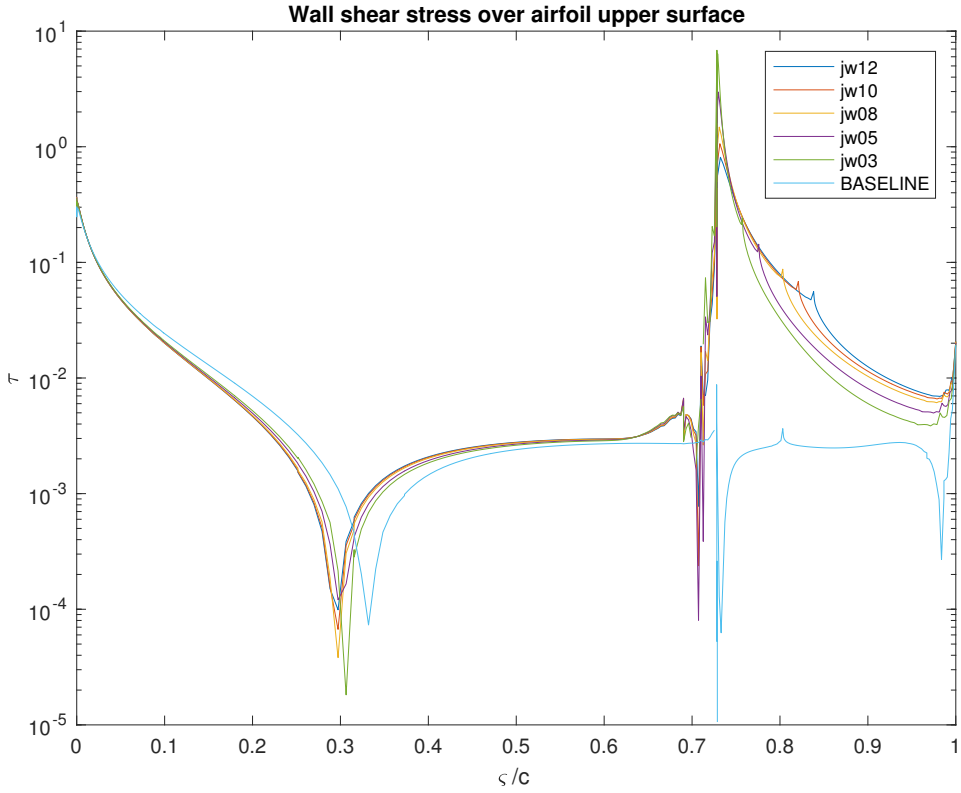

Figure 5.7: Jet width impact on the wall shear stress over airfoil upper surface

From figure 5.7 several conclusions can be reached. The first one, regarding the first boundary layer detachment and comparing with the baseline case (represented in cyan blue) is that the first detachment is produced slightly before, approximately a 3% of the chord, but is also relevant issue to take into consideration that the baseline case was not a stationary response and that this value could experiment some variation. The second one and the most remarkable is the increase on the wall shear stress after the jet actuation, this confirms the reattachment shown in the vorticity contour in figure 5.6. In addition, the wall shear stress increases with the jet width what indicates that the flow speed in the tangential direction of the airfoil in this region is higher as the jet width is increased, confirming the diffusion effect previously observed in figure 5.6.

This behaviour after the jet injection may seem contradictory with the reduction of the viscous drag previously shown in figure 5.5. The reduction has to come from the upper surface before the jet where a slight reduction of the wall shear stress is observed and also from the suction peak right after the jet, that is reduced with the width.

In the pressure coefficient distribution the increase of the wall shear stress downstream the jet region should be translated into an increase of suction. With the figure 5.8 this behaviour and the overall distribution will be analyzed.

The pressure distribution over the airfoil surface in figure 5.8 shows how in the upper surface the pressure is reduced, enhancing the suction effect and thus the lift. Over the lower surface the pressure is increased, contributing also positively to the lift . In this sense, although the differences are hardly noticeable (see figure 5.9(a)), the actuation that achieves the best suction is the one with 0.8% and the worst is the 0.3%, if the width is increased to the maximum value tested the suction decreases slightly. In the lower surface a higher pressure and thus a higher contribution to the lift is also achieved by the 0.8% jet and the same trend than in the upper surface is followed.

This pressure differences are able to explain the lift increase (in figure 5.3 until the 0.8% jet width where the major improvement is achieved, but the lift continues increasing until the 1%, the reasons to explain the further improvement have to be related with the jet downstream region.

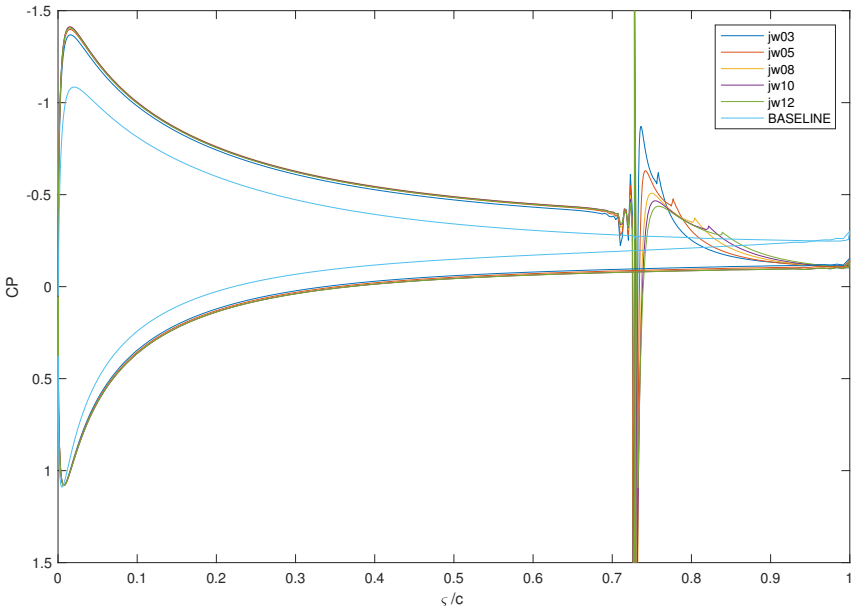

Figure 5.8: Jet width impact on the pressure distribution over airfoil surface

In relation with the behaviour shown in the wall shear stress 5.7 a suction increase in the jet downstream region was expected, compared with the baseline case it is not exactly the expected result, but taking into account that with the actuation the lower surface has a higher pressure this can not be assessed as detrimental, in fact is quite the opposite.

Comparing between cases with jet injection (shown in figure 5.9(b)) the situation is more complicated, firstly a suction peak is observed, this is caused due to the high velocities at the jet nozzle. As the jet width gets narrower, which implies a higher exit velocity, the suction peaks become larger, but a little further downstream the situation is reversed and as the jet width is increased the suction achieves to get stabilized sooner into higher values.

An integration may be needed to confirm the increase of the suction all over the whole jet downstream region, but taking into account that the pressure drag (previously shown in figure 5.5) increases even for the widest value and that also the lift increases beyond a 0.8% of jet width it makes sense to affirm that an augment of suction is produced if the jet width is increased.

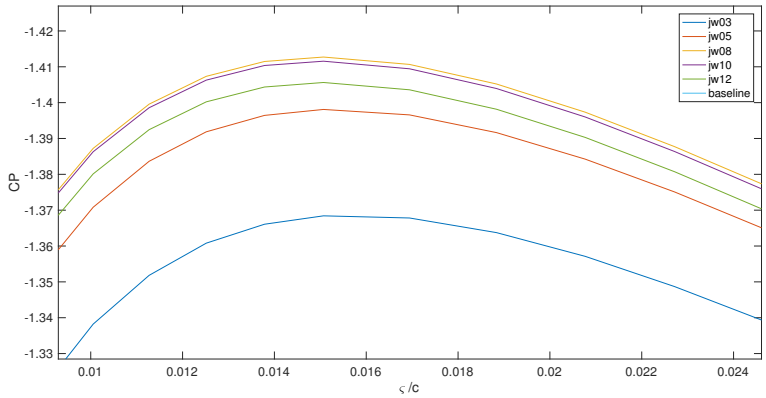

(a) Upper surface before jet injection

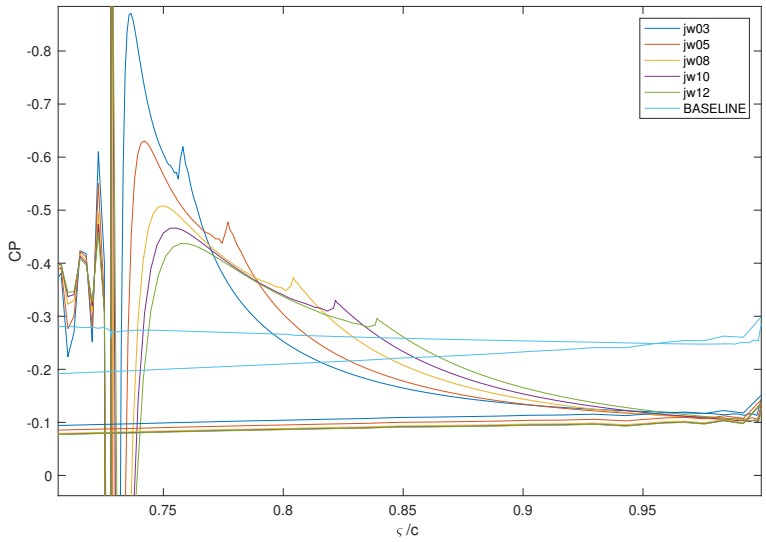

(b) Downstream jet region

Figure 5.9: Detailed regions of the pressure distribution

5.3.2. Jet angle study

In this study as explained above, the angle in which the fluid is injected having as a reference the chord line will be modified to asses its effect on the different aerodynamic characteristics. Having studied the influence of the jet width, the starting point of this study is setting a common jet width for all the simulations. On this matter the decision taken is using a jet width of 0.8% of the chord, because even though the best jet width tested in terms of efficiency was the widest one, the benefits of increasing the width from the chosen value to the maximum tested were not so noticeable as in the first stages. In addition, if a jet of 1.2% was used the change on the airfoil geometry would have a considerable influence on the aerodynamic performance if the angle of attack is reduced.

Reviewing the conditions for this study the jet will be placed at a 73% of the chord, the C_μ will be kept at 7% and the jet width will be a 0.8%. The initial jet angle γ will be 90^o, the same that in the previous section and will be reduced in steps of 10^o.

The results for the lift and drag coefficients while decreasing the jet angle are shown in the following figures 5.10 and 5.11.

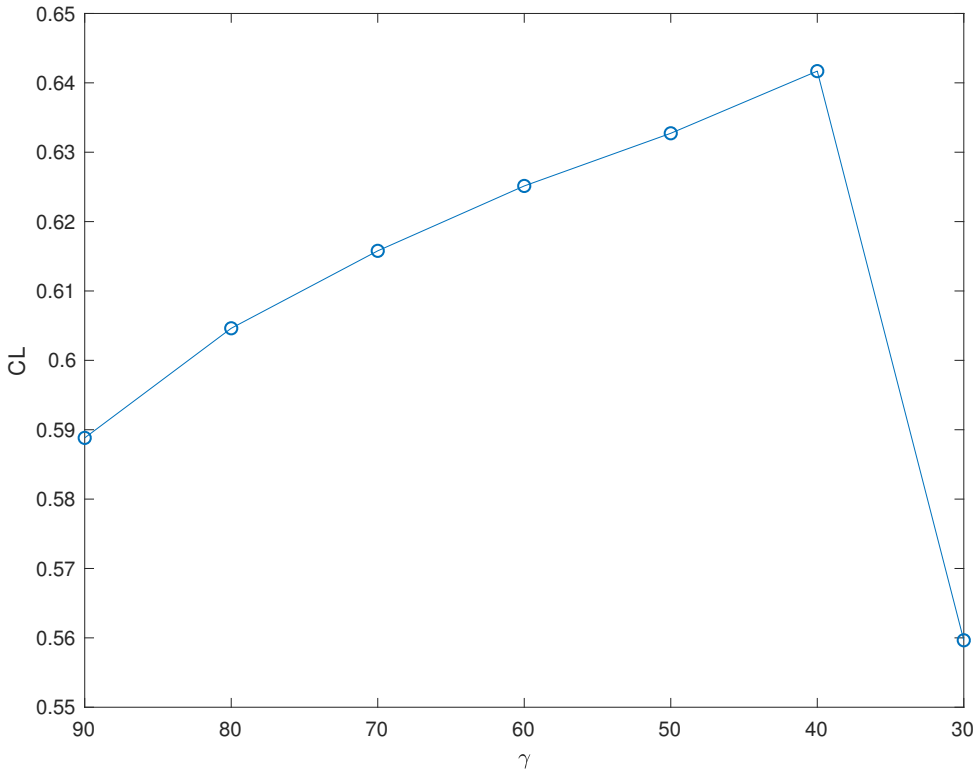

Figure 5.10: Lift coefficient variation with jet angle

The lift coefficient increases its value almost linearly from the initial 90^o angle until it reaches 40^o, then there is a maximum in 40^o and at 30^o the lift coefficient drops drastically under the initial tested value. The total improvement achieved corresponds to a 8.9% having as a reference the initial 90^o actuation that was already improved with an increased jet width.

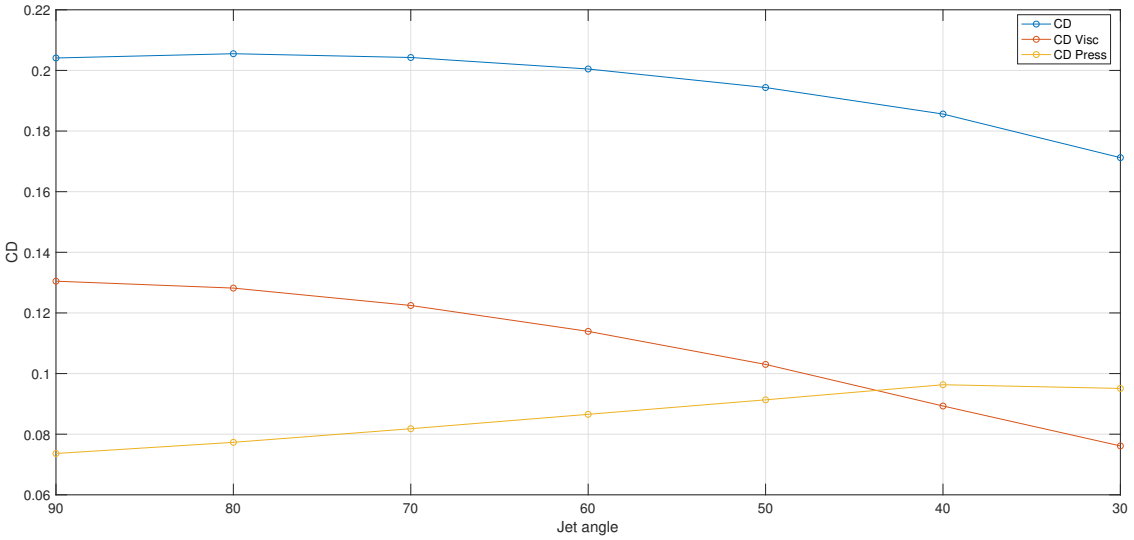

Figure 5.11: Pressure drag coefficient variation with jet angle

The drag coefficient in contrast with the lift suffers firstly a minor increase during the first ten degrees and then a considerable decrease. From the 40^o angle on, no unexpected results are obtained as in the previous graphic, the drag continues its decrease. The improvement achieved for the 40^o jet angle is a 9%, the improvement for the 30^o angle will not be considered due to its negative impact on the lift.

In the viscous and pressure drag analysis similar results as in the jet width study are expected, at least until the 40^o actuation.

The viscous drag also suffers a considerable decrease but now from the starting point, again the decrease of the viscous drag is not translated to the overall drag, the pressure coefficient will have something to do with this behaviour. The total improvement until gamma reaches 40^o is a 31,6%, a higher decrease compared with the jet width improvement.

The pressure drag shows a similar behaviour than the lift coefficient, a linear increase until 40^o and then drops slightly until the last angle tested. The reason for this increment in the pressure drag, taking into account that there is also a lift improvement can not be that the flow is less capable of following the airfoil shape. It may be related with a decrease of the pressure on the rear part of the airfoil caused by the higher velocities imposed by the jet, this issue has been later analyzed in detail with a pressure distribution plot.

5.3.2.1. *Vorticity and streamlines analysis*

Comparing the vorticity contour and the streamlines for a jet angle of 60^o in figure 5.12(a) with the ones from the jet width study at 90^o shown in figure 5.6 it can be deduced that injecting fluid in a more surface-normal direction can extend the effect of attraction produced by the low pressure of the jet to outer layers of detached flow with a higher pressure and moreover the velocity of the boundary layer in the downstream jet region seems to be reduced.

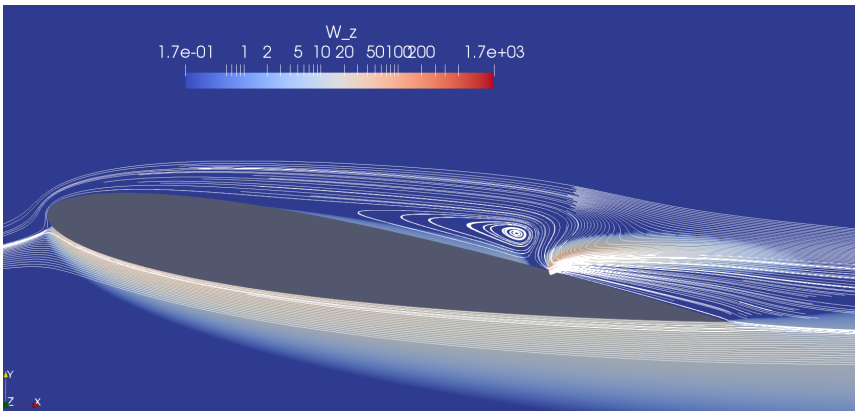

(a) Jet angle 60^o

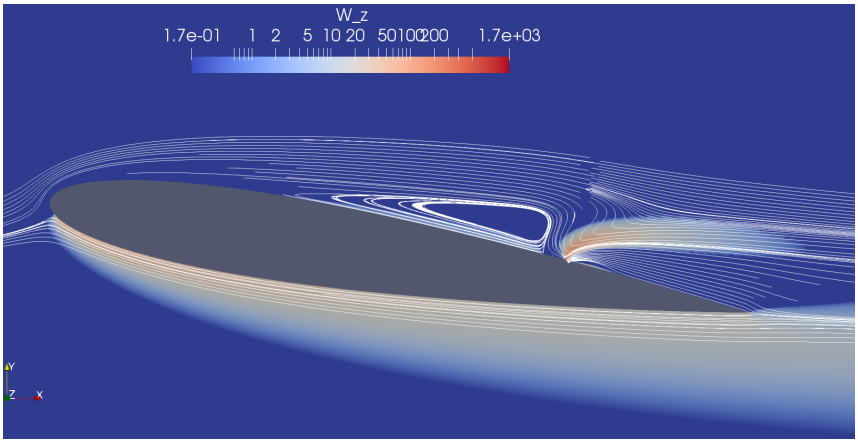

(b) Jet angle 40^o

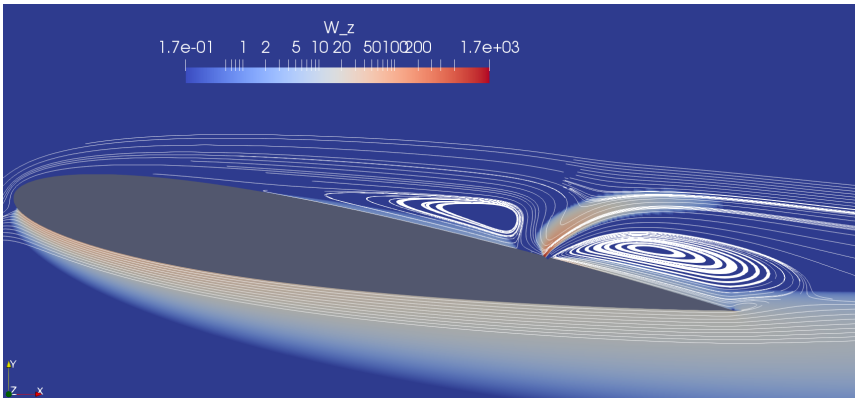

(c) Jet angle 30^o

Figure 5.12: Vorticity contour and streamlines for a jet angle of 60^o, 40^o and 30^o

This behaviour has a limit in which the lift coefficient drops drastically, with the figures 5.12(b) and 5.12(c) the causes of this phenomenon have been analyzed.

For a jet angle of 40º the maximum effectiveness of the jet is achieved. The increased angle attracts flow from the outer layers that were already detached while right after the jet slot the flow has the enough kinetic energy to keep attached to the airfoil surface overcoming the adverse pressure gradient, in fact at this angle a tiny separation bubble is formed just after the jet.

On the contrary, for a jet angle of 30º the velocity component in the tangential direction of the airfoil is not enough to compensate the adverse pressure gradient. As a result, a separation bubble is formed all over the downstream region from the jet until the trailing edge, but the overall response is still stationary. This phenomenon is known as boundary layer tripping, the jet angle and intensity trip the boundary layer so that it can not reattach.

To prove this results numerically a wall shear stress an a pressure coefficient plot are necessary. During the first stages of the actuation, between 90º and 50º, no substantial changes are expected only in the jet downstream region. In the 40º actuation the tiny separation bubble should appear in the wall shear stress plot with a peak and for the 30º actuation a reduction of the suction on the airfoil's upper surface in the pressure coefficient plot is expected.

5.3.2.2. Wall shear stress and pressure distribution analysis

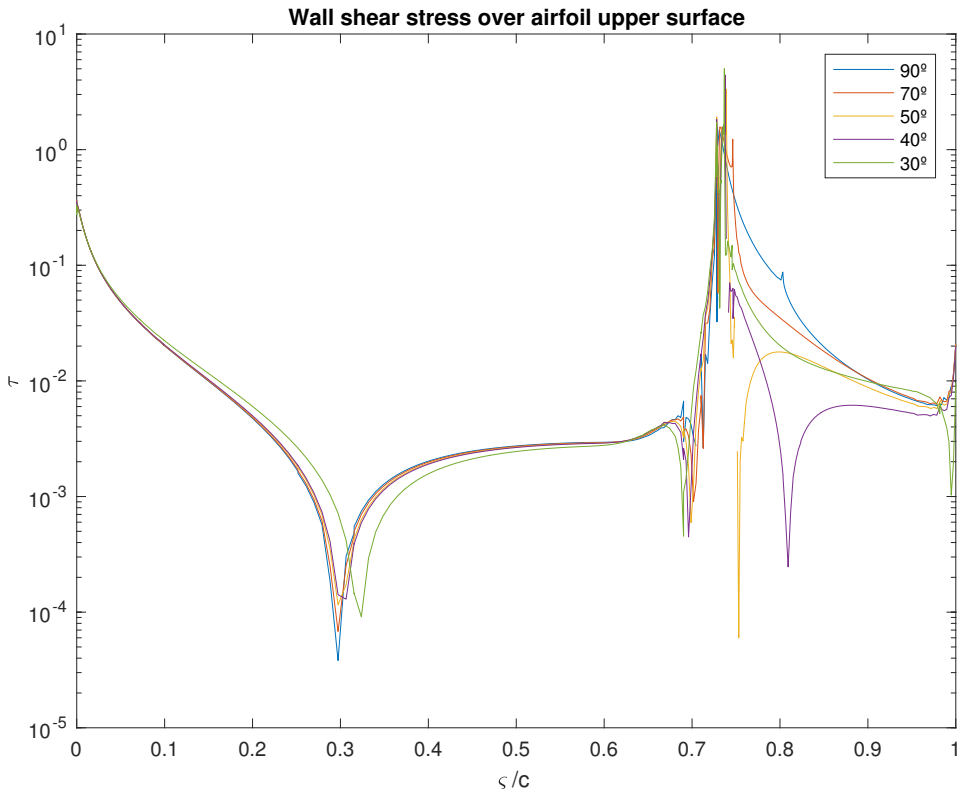

Figure 5.13: Jet angle impact on the wall shear stress over airfoil upper surface

The wall shear stress plot in figure 5.13 shows from 90^o to 50^o, a reduction of the friction over the jet downstream region. For the 40^o case, represented in purple, the reduction achieves its maximum, since a this angle the lowest velocity in which the flow reaches the trailing edge attached to the surface. A separation bubble is also represented at a 76% of the chord confirming the detachment shown at figure 5.12(b).

Finally, in the 30^o case represented in green the wall shear stress shows similar values to the ones from the first angle reductions, in this case of separated region the friction is acting in the upstream direction, so when analysing the viscous drag as the ”area” below the curve, this region has to be in fact subtracted from the total friction drag.

In conclusion, reducing the gamma angle is translated into a reduction of the velocity of the boundary layer in the wall proximity of the reattached region and therefore the normal velocity gradients and the friction are reduced.

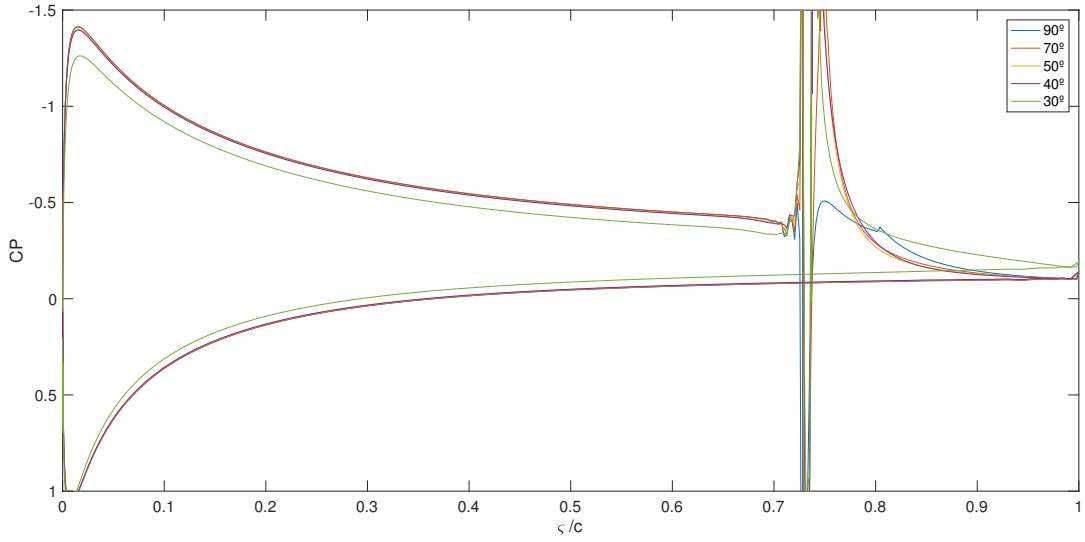

Figure 5.14: Jet angle impact on the pressure coefficient

The pressure coefficient plot shows almost no differences in the range of 70^o to 40^o. If it is compared to the quasi tangential case represented in blue, an increased suction region is observed from right after the jet until the 0.8 of the chord. As the gamma angle is reduced the peak becomes larger and although it is narrow in ’x’ is causing the lift improvement.

The 30^o case represented in green shows an overall decrease of the suction in the upper surface before the jet and also in the lower surface, therefore the resulting lift, that is the difference between the upper and lower surface pressure, suffers a decrease. In addition, the convergence of both lines is produced at a lower pressure, what indicates an acceleration of the flow in the lower surface, thereby confirming that there is fluid recirculating from the lower surface to the upper.

5.3.3. Blowing jet results summary

5.3.3.1. Jet width

It has been proved that increasing the jet width improves the performance of the jet since its instability effect range is extended. The viscous drag in the upper surface before the jet and right after the jet is decreased, but downstream the jet region it increases, nevertheless the overall drag balance is positive. A lift increase is produced due to an improvement of the pressure distribution over both upper and lower surfaces until the jet width reaches a 0.8%, from that point on the increased suction downstream the jet region achieves to maintain increasing the lift until the 1% of jet width and then it starts to decrease. In the table below 5.3.3.1. a summary of the results is shown.

Jet width	CL	CD	CD_{press}	CD_{visc}	E
Baseline	0.3748	0.1527	0.0773	0.0754	2.454
0.3%	0.5518	0.2151	0.0539	0.1611	2.565
0.5%	0.5741	0.2092	0.0658	0.1434	2.744
0.8%	0.5888	0.2041	0.0736	0.1305	2.884
1.0%	0.5914	0.2016	0.0756	0.1251	2.933
1.2%	0.5906	0.1994	0.0785	0.1209	2.961

Table 5.3: Aerodynamic characteristics for the jet width study

5.3.3.2. Jet angle

Increasing the jet angle in the normal direction of the airfoil surface improves both lift and drag. The suction at the jet region is enhanced until the gamma angle reaches 40^o, for lower degrees a boundary layer tripping is produced. Moreover the viscous drag on the jet downstream region is reduced thanks to a decrease of the velocity of the boundary layer. From the baseline case the lift has achieved an improvement of a 71.2% and the drag has augmented a 21.5%. In the table 5.3.3.2. the results have been summarized.

Jet angle	CL	CD	CD_{press}	CD_{visc}	E
Baseline	0.3748	0.1527	0.0773	0.0754	2.454
90^o	0.5888	0.2041	0.0736	0.1305	2.884
80^o	0.6046	0.2055	0.0773	0.1282	2.942
70^o	0.6158	0.2043	0.0818	0.1225	3.01
60^o	0.6251	0.2005	0.0866	0.1139	3.12
50^o	0.6327	0.1944	0.0913	0.1030	3.17
40^o	0.6417	0.1856	0.0963	0.0893	3.46
30^o	0.5597	0.1712	0.0951	0.0761	3.26

Table 5.4: Aerodynamic characteristics for the jet angle study

5.4. Suctioning Jet

The aim of this section of the study is once having obtained the maximum profit from the blowing jet changing its physical parameters, determining if these changes can be extrapolated to a suctioning jet configuration, that in advance should be more effective since the suction removes the low momentum region of the boundary layer, turning it more enduring to separation.

The baseline parameters for this actuation and common for all the simulations will be the same used during the blowing jet study.

- C_μ = 7%
- Jet position: 73% of the chord.

In relation with the jet parametrisation for this case will be kept unchanged as it was previously explained in section 5.2., the only needed change is to invert the fluid injection direction when the boundary conditions are applied.

To start with this study, as we do not have previous references of the results that can be obtained a single simulation will be carried establishing the parameters that were found more effective in the blowing jet study.

- Jet width: 0.8%
- Jet angle: 40^o

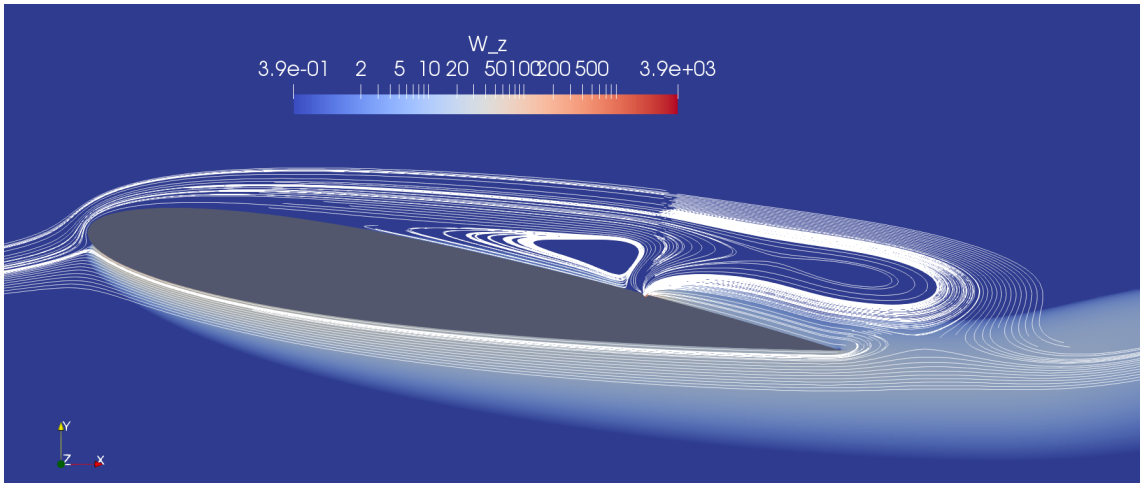

Figure 5.15: Vorticity contour and streamlines for a suctioning jet with 0.8% of jet width and 40^o of jet angle

In the vorticity contour and streamlines figure 5.15 it can be appreciated that the suctioning jet is not able to completely reattach the flow after its actuation, since there is a recirculation from the lower surface to the upper in the trailing edge region. Moreover the response is not stationary, a vortex street can be observed in the wake. In the figure the instant with maximum lift coefficient has been represented.

The aerodynamic performance of the actuation is summarized and compared with the blowing jet best result in the table 5.4. below:

Actuation type	CL	CD	CD_{press}	CD_{visc}	Amp.	f_o	E
Baseline	0.3748	0.1527	0.0773	0.0754	0.0202	0.89	2.454
Blowing (40^o & 0.8%)	0.6417	0.1856	0.0963	0.0893	0	0	3.46
Suctioning (40^o & 0.8%)	0.6054	0.2196	0.1411	0.0785	0.0379	0.94	2.75

Table 5.5: Aerodynamic characteristics for the suctioning jet study

As expected considering the results obtained at figure 5.15 the aerodynamic characteristics for the suctioning jet maintaining the same momentum coefficient have suffered a deterioration. Specially the pressure drag coefficient shows a noticeable increase due to the detachment and recirculations at the trailing edge region.

5.4.1. Jet width study

In order to verify that the jet width increase also affects positively to the airfoil performance in the case of a suctioning actuation, a single simulation has been performed. Its time averaged results are presented in table 5.4.1. A reduction of the jet width using the same parameters than in the previous section should show worse results confirming this tendency.

Jet width	CL	CD	CD_{press}	CD_{visc}	E
Baseline	0.3748	0.1527	0.0773	0.0754	2.45
0.8%	0.6054	0.2196	0.1411	0.0785	2.75
0.5%	0.5618	0.2198	0.1416	0.0782	2.55

Table 5.6: Aerodynamic characteristics for a suctioning actuation with 0.8% and 0.5% of jet width and 40^o of jet angle

The lift coefficient is the most negatively affected in this case, whereas the drag coefficient shows almost no difference. The reason for this changes are that in the case of a suctioning actuation the natural behavior of the suction does not introduce a jet or a stream of fluid able to affect the drag in the downstream jet region. Moreover a reattachment is not achieved in both cases so the lift improvement for the increased width must be due to the same reasons that in the blowing case, an extended range of the suctioning effect.

5.4.2. Jet angle study

To asses the effect of the jet angle in the suctioning actuation several simulations have been performed changing this parameter in steps of 20^o. The jet width has been also fixed to a 0.8% as it was shown as the most effective.

What we expect with this modifications is to find whether there is or not an angle that is able to completely reattach the flow in the jet downstream region. As the results are not stationary a Fourier transform has been applied to obtain mean values, they are as follows:

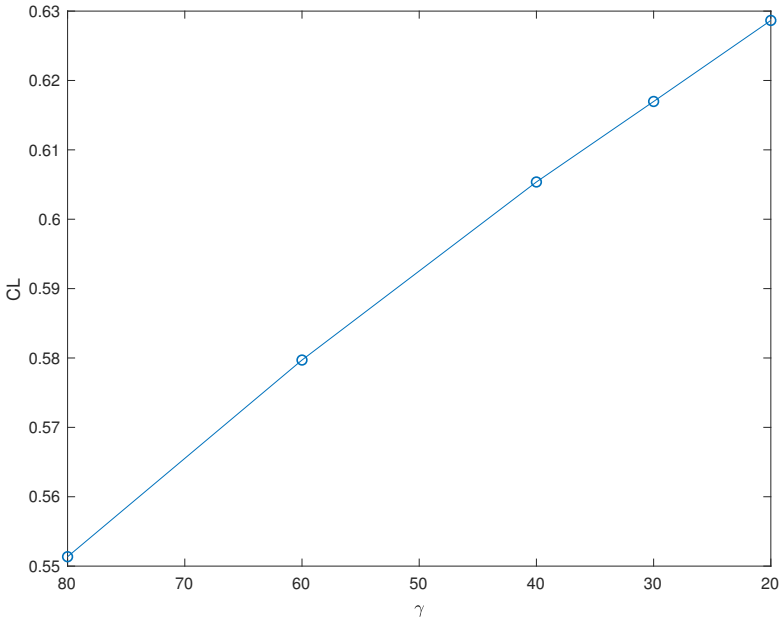

Figure 5.16: Jet angle impact on the lift coefficient

The lift coefficient experiments a linear increase as the jet angle is modified to a surface normal direction. In contrast with the blowing actuation no sudden deterioration is observed when the jet angle is increased below 40 degrees. Among the reasons to explain this behaviour is the fact that with the suction there are no artificial velocity components of the jet in charge of counteracting the adverse pressure gradient that is causing the detachment, is the suction itself that has to reattach and re-energize the boundary layer.

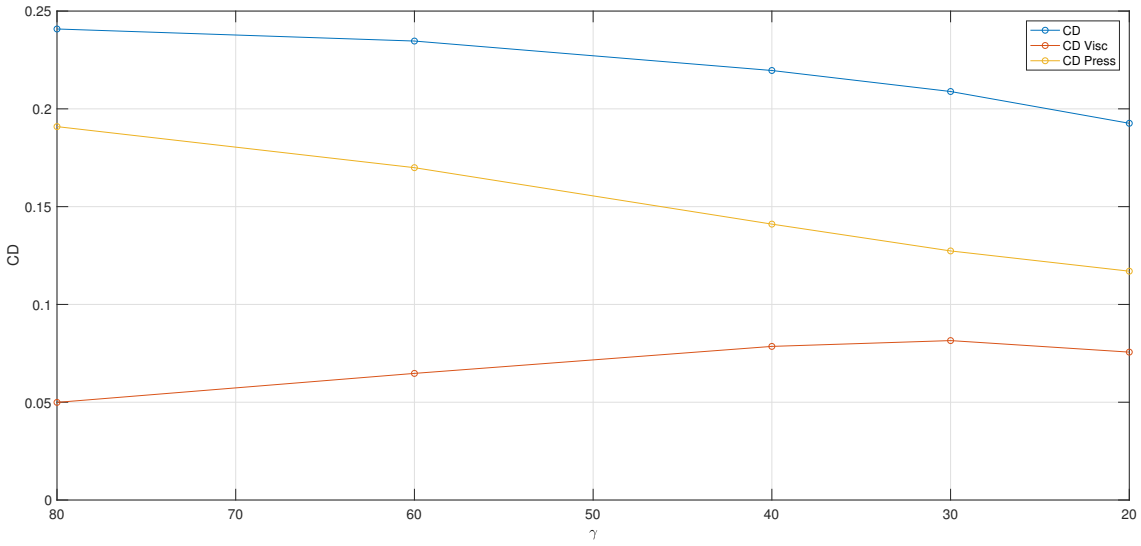

Figure 5.17: Jet angle impact on the drag coefficient

The drag coefficient decreases as the jet is increased into a surface normal direction approximately a 20% comparing the 80º actuation with the lowest one. The reasons to explain this improvement are probably that with this modification the suction at the jet region is able to reattach more flow obtaining a cleaner wake region. The decrease of the pressure drag and the increase of the viscous coefficient supports this hypothesis.

5.4.2.1. Vorticity and streamlines analysis

A vorticity contour and streamlines is useful to visualize and understand what is actually happening when the jet angle is increased. In figure 5.18 the two extreme cases (the 20º and the 80º) at its maximum lift coefficient instant are represented. The first separation bubble has the same characteristics in both cases, is in the jet slot region where more differences are found, for the jet angle of 80º the flow is forced to make a sharp turn before being suctioned in the jet cavity whereas in the 20º this turn is smoother. The recirculation of the trailing edge region seems also to be slightly improved with respect the 80º actuation. A pressure coefficient and a wall shear stress plot will be later used to verify the hypothesis.

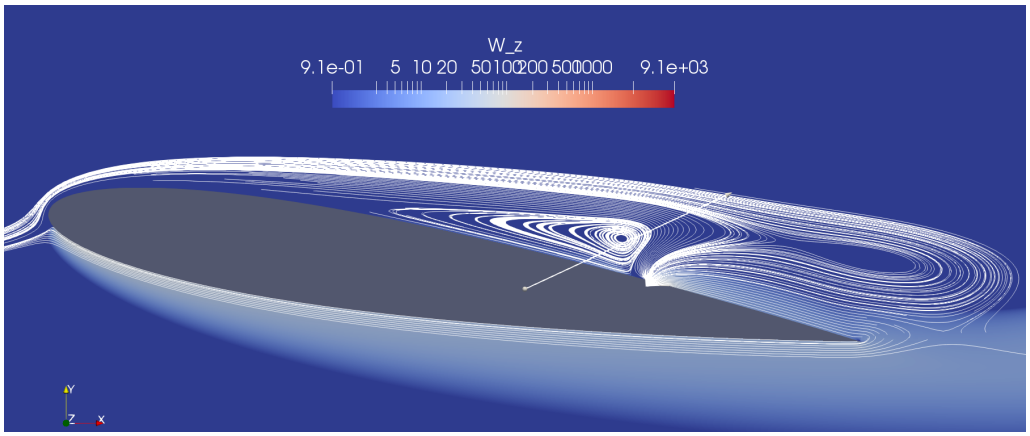

(a) Jet angle 80º

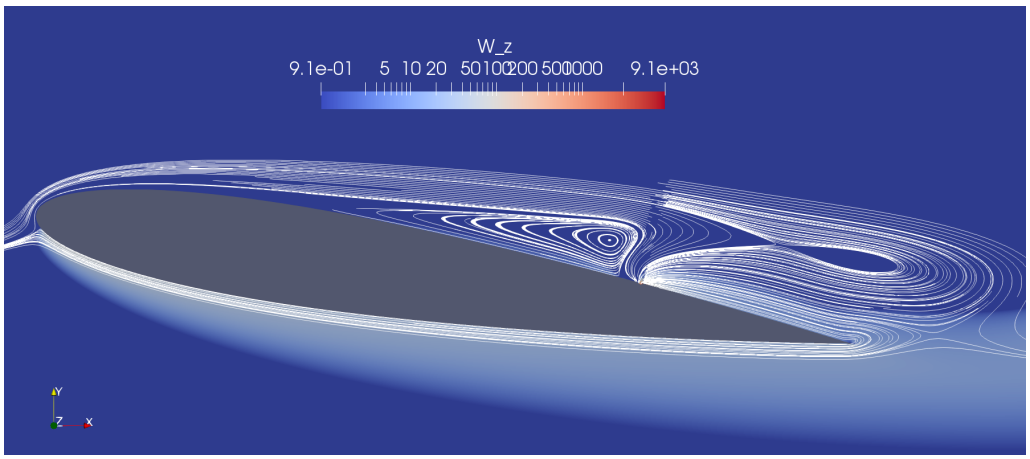

(b) Jet angle 20º

Figure 5.18: Vorticity contour and streamlines for a jet angle of 80º and 20º. Maximum lift coefficient instant.

5.4.2.2. Wall shear stress and pressure distribution analysis

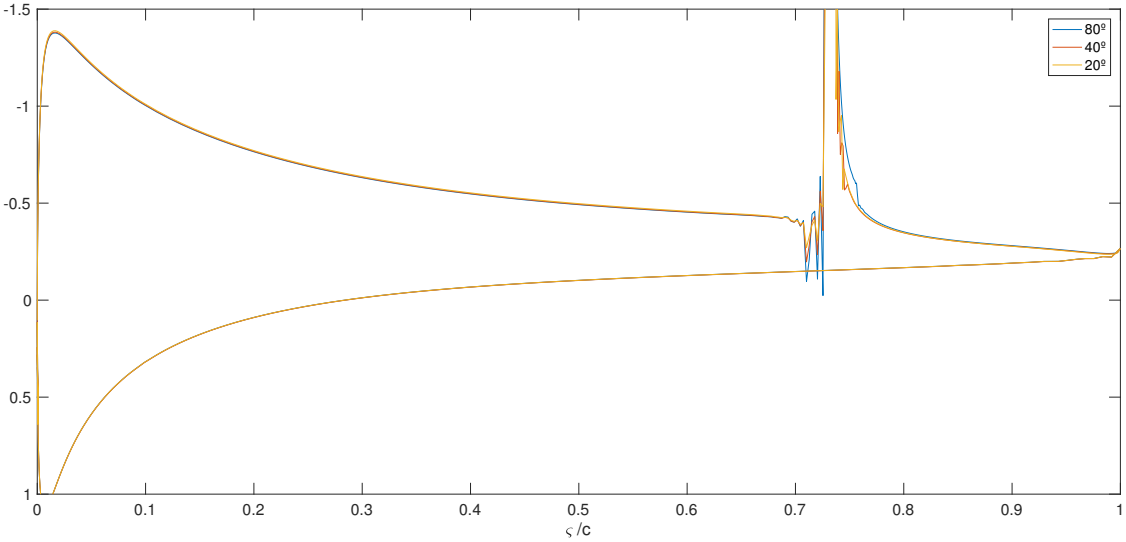

Figure 5.19: Jet angle impact on the pressure coefficient for a suctioning jet

The pressure distribution represented in figure 5.19 corresponds to the maximum lift coefficient instant. Almost no differences are shown in between simulations with different jet angles, the pressure distribution on the lower and upper surface excluding the jet slot region are the same. The increase of lift comes then from an increase of suction in the jet slot region, that although narrow in 'x' entails a large area, the figure 5.20 below shows this region zoomed.

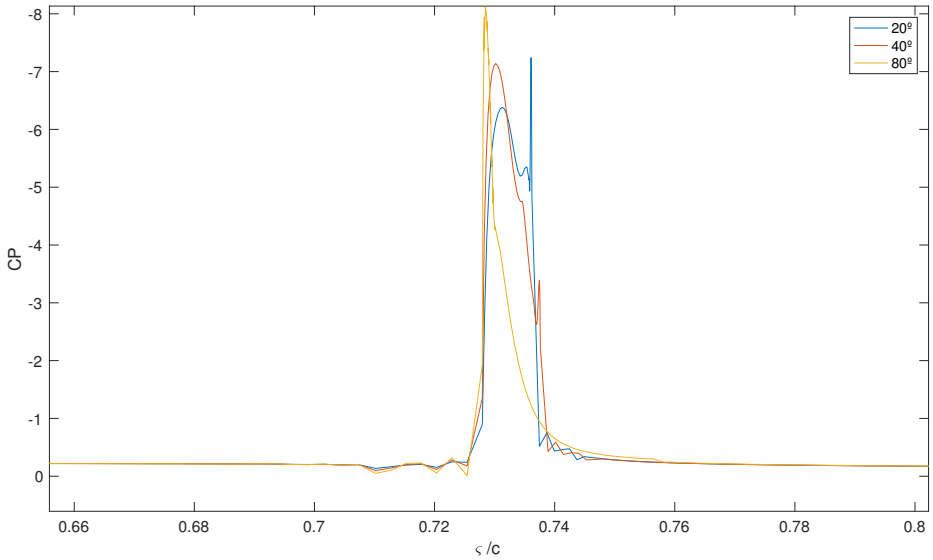

Figure 5.20: Pressure distribution zoom at the jet slot region

The wall shear stress plot shown in figure 5.21 also shows almost no differences in between simulations, which indicates that the velocity distribution is almost the same, and again only changes in the jet slot region, where the logarithmic scale may be hiding the peaks that could explain the viscous drag increase.

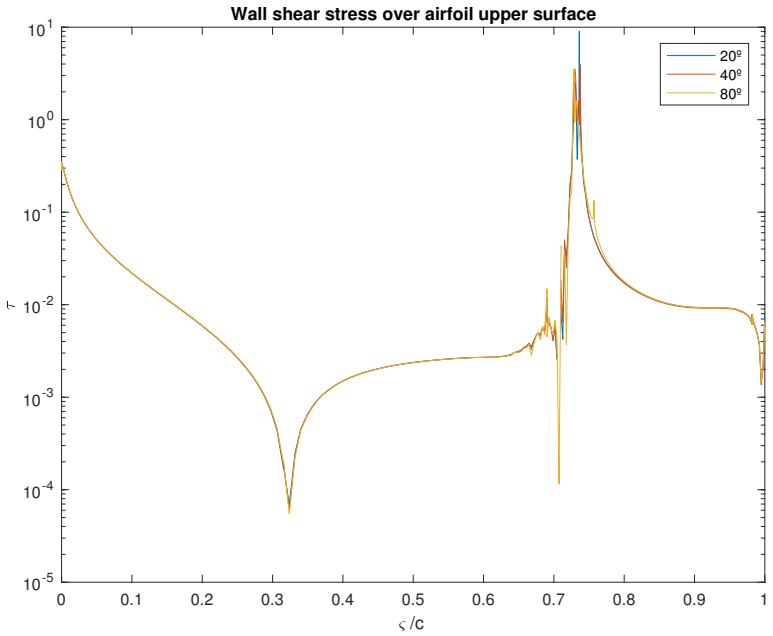

Figure 5.21: Jet angle impact on the wall shear stress coefficient for a suctioning jet

The best results for the suctioning jet are summarized in the table below 5.4.2.2.. The increase of the jet width has been proved to be also positive in the suctioning actuation for the same reasons than the blowing jet. In relation with the jet angle, the best angle tested was the 20 degree actuation, but in this case there are no reasons to expect a detachment if the angle is increased to a completely surface normal direction which could not be tested due to mesh limitations. The lift coefficient has achieved a maximum improvement of a 67.7% and the drag has augmented a 26.1% from the baseline case.

Jet angle	CL	CD	CD_{press}	CD_{visc}	E
Baseline	0.3748	0.1527	0.0773	0.0754	2.45
80^o	0.5514	0.2408	0.1909	0.0499	2.28
60^o	0.5797	0.2347	0.1699	0.0647	2.47
40^o	0.6054	0.2196	0.1411	0.0785	2.75
30^o	0.6170	0.2089	0.1274	0.0815	2.95
20^o	0.6287	0.1926	0.1170	0.0756	3.26

Table 5.7: Aerodynamic characteristics for a suctioning actuation with 0.8% of jet angle

5.5. Synthetic Jet

As it was explained in the theoretical background section a synthetic jet is a zero net mass flux actuator that alternately ingests and expels fluid. This means that this actuation is a combination of the two previous studies, blowing and suctioning. Having determined the parameters that maximize the efficiency in both cases it will be now applied to this study with the aim of combining the benefits of each actuation.

The parameters defining the jet geometry in this study will be the following:

- Jet angle: 40^o
- Jet width: 0.8%

The jet width increase was shown to be effective in both actuation, so it will be maintained. In contrast, the jet angle showed different behaviours; for the blowing the maximum efficiency was at 40^o and suffered a drop below, whether for the suction a surface normal direction was the optimum. Setting a 40^o angle is a good trade-off since it gathers benefits for both actuation.

5.5.1. Synthetic jet parametrisation

The momentum coefficient definition for this type of actuation has to be modified since now the fluid injection is not steady, is oscillatory. The C_μ is defined as follows:

$$C_\mu = \frac{\bar{I}_j}{\frac{1}{2}\rho_\infty U_\infty^2 c} \tag{5.5}$$

where $\bar{I}_j$ is the time averaged jet momentum per unit length during the outstroke.

$$\bar{I}_j = \frac{1}{\tau}\rho_j b \int_0^\tau u_j^2(t)dt \tag{5.6}$$

where $\tau = \frac{T}{2}$, T is the period of the jet oscillation, ρ_j is the jet density, b is the jet orifice width, and $u_j(t)$ instantaneous jet-width-averaged velocity.

The instantaneous jet-width-averaged velocity corresponds to the maximum (along one period) jet-width-averaged velocity $\bar{u_j}$ multiplied by a cosine with period $T = 2\tau$, being now $\bar{I}_j$:

$$\bar{I}_j = \frac{1}{\tau}\rho_j b \int_0^\tau \bar{u_j}^2 cos^2(\frac{\pi}{\tau}\cdot t))dt \tag{5.7}$$

Performing the integral and considering incompressible flow finally the momentum coefficient leads to:

$$C_\mu = b \cdot \bar{u_j}^2 \tag{5.8}$$

Maintaining the same parabolic velocity profile at the jet exit plane used at section 5.2. the jet maximum velocity u_{Jmax} is the following:

$$u_{Jmax} = \frac{3}{2}\sqrt{\frac{C_\mu}{b}} \tag{5.9}$$

The boundary conditions to be applied in the jet slot have now to consider an oscillating fluid injection, it has been done introducing a time dependent condition in the solver to the following equations for each velocity component:

$$u = (Ax^2 + Bx + C) \cdot u_{Jmax} \cdot cos(2\pi f_{jet} \cdot t) \cdot cos(\gamma + \frac{\pi}{2}) \tag{5.10}$$

$$v = (Ax^2 + Bx + C) \cdot u_{Jmax} \cdot cos(2\pi f_{jet} \cdot t) \cdot sin(\gamma + \frac{\pi}{2}) \tag{5.11}$$

5.5.2. Synthetic Jet results

Once having redefined the momentum coefficient and the boundary conditions for a zero net mass flux actuation there are also other parameters that have to be defined. One of them is the jet frequency of oscillation, in the previous research it was found effective for a sweeping jet actuation setting a frequency equal or double to the vortex shedding frequency.

Other parameter that has to be adjusted is the momentum coefficient value, that in the previous sections of the study it was set to a 7%, a value that is in fact almost unreachable for this type of mechanical actuator since it does not introduce fluid by means of a bleeding system. Instead a more realistic value around a 1% has been be used.

5.5.2.1. Momentum coefficient

The first set of simulations have been performed in the direction of assessing the impact of the momentum coefficient on this type of actuation. The maximum C_μ tested has been a 1% and the minimum a 0.5%, below this value the jet exit velocity is almost the flow stream velocity and would have no sense to reduce it below. The jet frequency has been fixed to the natural vortex shedding frequency f_o.

- $C_\mu = 0.5\% - 1\%$
- $f_{jet} = f_o = 0.892Hz$

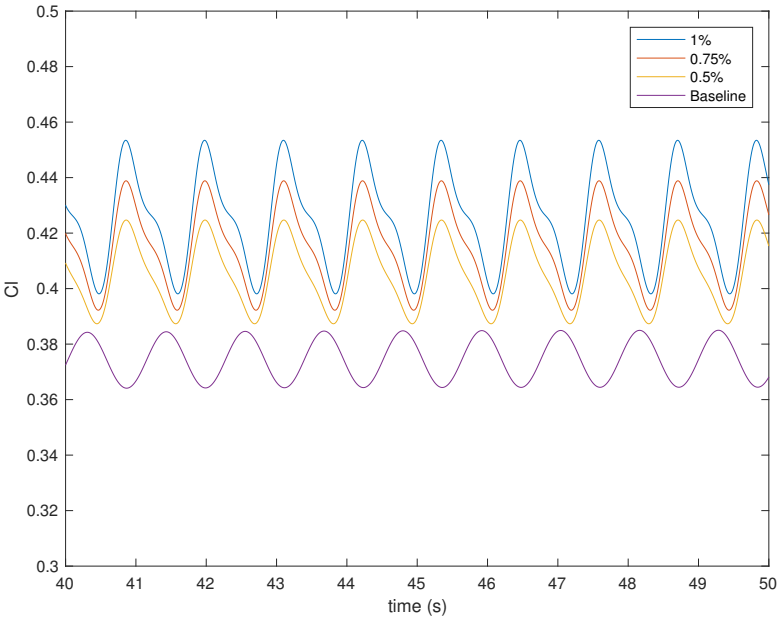

Figure 5.22: Lift coefficient time response for a synthetic jet with jet frequency f_o, jet angle 40^o and jet width 0.8%

In figure 5.22 the momentum coefficient impact on the lift for a synthetic jet is shown. It can be clearly appreciated that as the momentum coefficient is increased the lift improves, this was the expected behaviour because what it has been actually done is introducing more energy to the each suctioning and blowing cycle that were already proven to be effective. From the figure it can be also appreciated that the actuation does not achieve a stationary response, so the vortex shedding has not been suppressed and in fact has the same frequency. In addition the amplitude of the oscillation becomes greater as the momentum coefficient is increased.

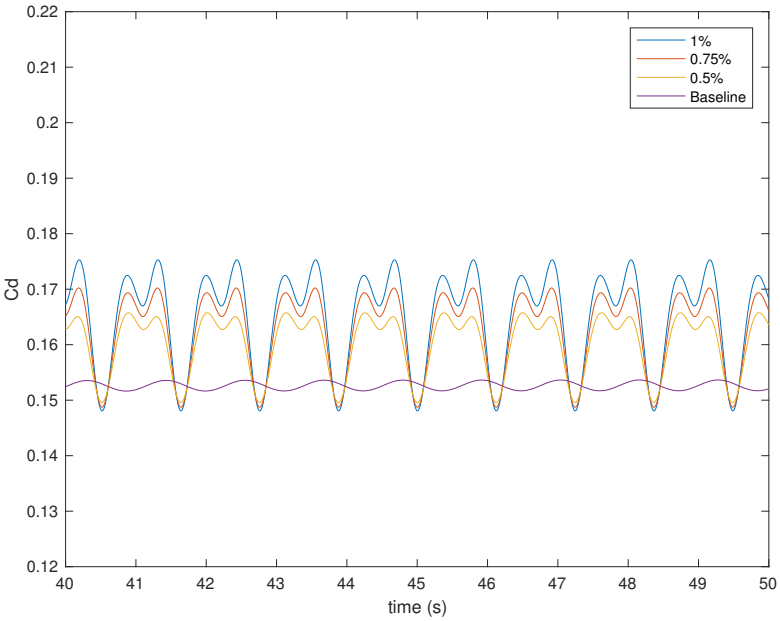

Figure 5.23: Drag coefficient time response for a synthetic jet with jet frequency f_o, jet angle 40^o and jet width 0.8%

For the drag coefficient shown in figure 5.23 a similar response than for the lift is obtained, the drag increases with the momentum coefficient and the amplitude of the oscillations becomes also grater.

In the table below 5.5.2.1. the averaged results have been summarized, the best results have been obtained for the 1% momentum coefficient. The lift coefficient has been improved a 13.5% and the drag has augmented a 8.1%.

C_μ	CL	$CL_{Amplitude}$	CD	CD_{press}	CD_{visc}	E
Baseline	0.3748	0.0202	0.1527	0.0773	0.0754	2.45
0.5%	0.4053	0.0374	0.1601	0.0827	0.0775	2.53
0.75%	0.4152	0.0466	0.1627	0.0844	0.0783	2.55
1%	0.4255	0.0553	0.1651	0.0862	0.0789	2.57

Table 5.8: Momentum coefficient impact on the aerodynamic performance

5.5.2.2. Jet frequency

The remaining parameter that can affect the jet performance is the jet frequency, that in the previous section was set to the vortex shedding frequency. Setting or finding a resonant frequency could contribute positively to delete the baseline vortex shedding behaviour of the airfoil, moreover this can be done without increasing the momentum coefficient and thus the energy introduced.

In the simulation a jet frequency equal to the double of the vortex shedding will be tested, the momentum coefficient will be the one that obtained the best results in the previous section, a 1%.

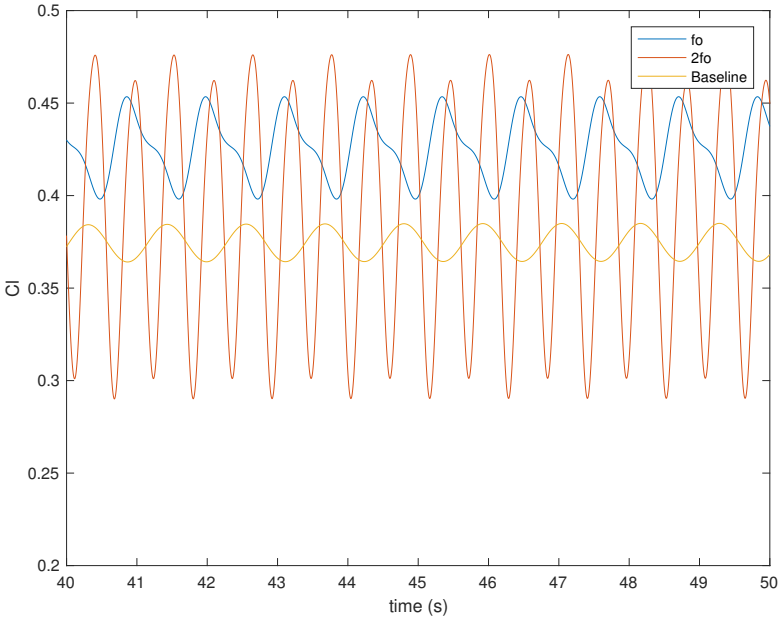

Figure 5.24: Lift coefficient time response for a synthetic jet with C_μ 1%, jet angle 40^o and jet width 0.8%

As it can be observed in figure 5.24 when the jet frequency is increased to $2f_o$ the amplitude of the oscillations increases substantially, concretely is about nine times bigger than the baseline case. Moreover the vortex shedding frequency of the airfoil has been also doubled with the jet frequency. This results would not be negative if the lift coefficient mean value would have stabilized in a higher value, but it is not the case, in fact the mean value is lower than the obtained with the actuation with frequency f_o.

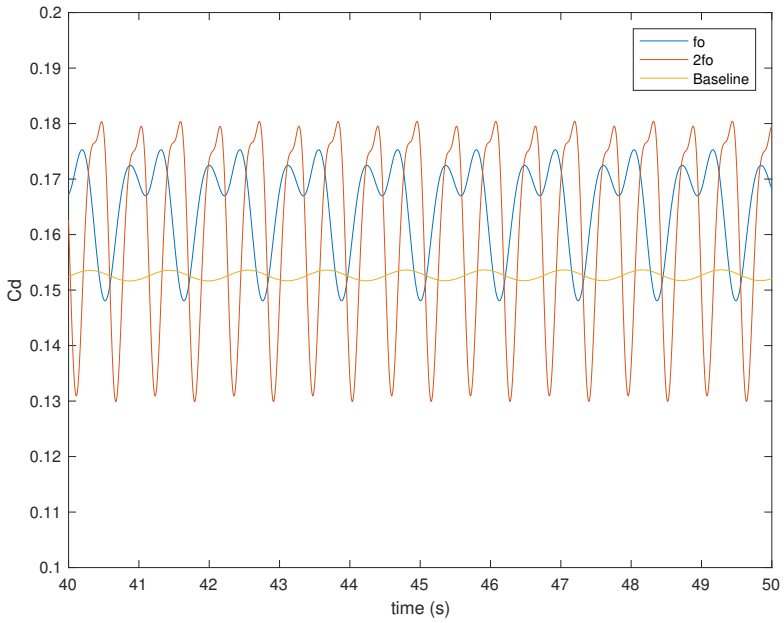

Figure 5.25: Drag coefficient time response for a synthetic jet with C_μ 1%, jet angle 40º and jet width 0.8%

For the drag coefficient the situation is not differing much from the lift case. The amplitude of the oscillations has also grown exaggeratedly, however as a positive note the mean value has decreased in comparison with the actuation with jet frequency f_o.

In the following table 5.5.2.2. the results have been summarized, but it has been proved that at this ultra-low Reynolds regime the turbulent effects that are searched while increasing the frequency do not achieve any benefit.

f_{jet}	CL	CD	CD$_{press}$	CD$_{visc}$	CL$_{Amplitude}$	E
Baseline	0.3748	0.1527	0.0773	0.0754	0.0202	2.45
f_o	0.4255	0.1651	0.0862	0.0789	0.0553	2.57
$2f_o$	0.3905	0.1607	0.0821	0.0786	0.1858	2.43

Table 5.9: Jet frequency impact on the aerodynamic characteristics for a synthetic jet

5.5.3. Synthetic jet comparison

In order to fairly compare the efficiency of the synthetic jet actuation with the blowing and suctioning jet a set of simulations using the same momentum coefficient will be carried. The momentum coefficient for all cases will be set to a 1% since it was established as the maximum that the synthetic jet could achieve, the common parameters for all the simulations will be the following:

- $C_\mu = 1\%$
- Jet angle: 40^o
- Jet width: 0.8%

The lift time response represented in figure 5.26 will be used to compare the efficiency of each actuation.

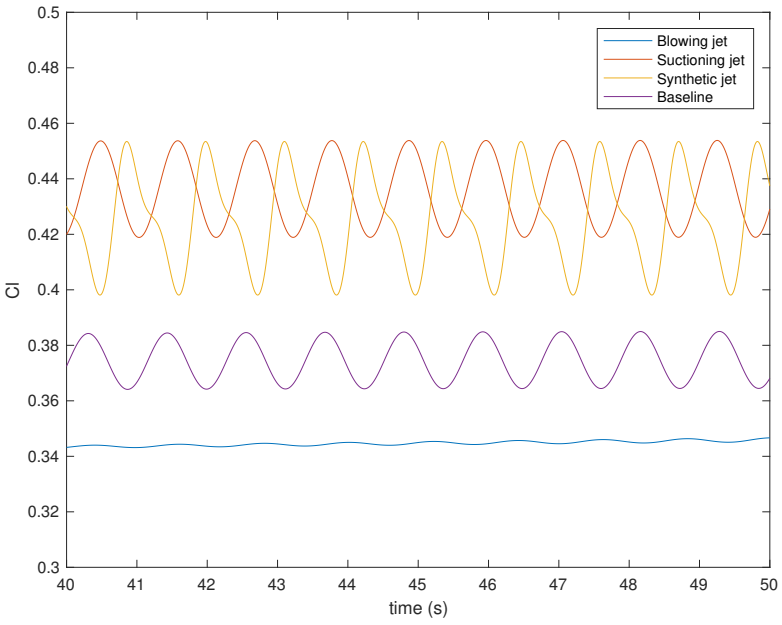

Figure 5.26: Lift coefficient time response for the three actuation in the study

The worst result is obtained by the blowing jet, that with this lower momentum coefficient injection is not able to improve the results, in fact it have been downgraded if compared with the baseline case. In contrast, synthetic jet and suction both achieve an improvement of the baseline characteristics, being the suction the most effective.

These results show that the behaviour and the efficacy of the different actuators depends also on the amount of energy supplied, if a low momentum coefficient is used the suctioning actuation appears as the best option over the synthetic jet.

CONCLUSIONS

In a previous research Active Flow Control techniques such as sweeping jets and synthetic jets applied in an ultra-low Reynolds regime (Re=1000) were found effective to prevent or retard flow detachment as well as reattach an already separated flow. These actuators achieved lift enhancements, but also induced a large skin-friction drag increase due to the high velocities near the airfoil surface. The aim of this study was to reduce the viscous drag while keeping lift enhancement. To achieve that the geometry of the actuators has been modified using two control parameters, the jet width and the jet angle in which the fluid is injected. These geometrical modifications have been applied to different jet configurations; blowing jets, suctioning jets and synthetic jets.

The first jet configuration that has been studied is the blowing jet. The jet width increase in this case has obtained positive results in terms of lift enhancement and drag reduction, the lower velocity of the jet stream has achieved a reduction of the viscous drag, specially in the upper surface before the jet slot region. In addition, the lift has improved due to an improvement of the pressure distribution over both upper and lower surfaces and due to an increase of the suction in the jet downstream region. The jet angle modifications have also delivered interesting results, a jet angle in which the lift coefficient is maximized has been found. Increasing the angle from tangential to a surface normal direction achieves to reattach or attract fluid from outer layers to the airfoil tangential direction, but as the jet angle is increased the velocity component that has to overcome the adverse pressure gradient at the airfoil's rear is also reduced, therefore there is a maximum jet angle that maximizes the lift coefficient.

In the suction study the jet width increase has also turned into a lift improvement, but the drag coefficient appeared unchanged. This outcome is related with the natural behaviour of the suction, in which there is no jet stream causing viscous drag and is the suction itself that produces the reattachment removing the low momentum of the boundary layer. The jet angle in this case had not a maximum, it increased linearly, being the surface normal direction the one that obtained the best results both for lift and drag.

The last jet configuration tested is the synthetic jet actuation, where the parameters that maximized the efficiency in the blowing and suction studies have been combined with the objective of obtaining the benefits of each actuation. In this actuation also other parameters played a significant role, which are the momentum coefficient and the jet frequency. At this ultra-low Reynolds regime a frequency increase beyond the vortex shedding frequency has been proved to be ineffective, destabilizing the response in the form of increased amplitude oscillations and reducing the lift to drag ratio. In contrast, the momentum coefficient increase has appeared as the only valid option to improve the efficiency.

With this study it has been proved that besides the momentum coefficient and the jet location the geometrical parameters of the actuator have also a considerable impact on the overall efficiency of the actuation, in particular for the blowing jet the lift has been improved a 16% and the drag has been reduced a 14% taking as reference the previous study results. In addition, it has been also proved that when it comes to choose in between different jet configurations the determining factor is the momentum coefficient, for lower momentum coefficients suction and synthetic jets are more effective than blowing whereas for higher momentum coefficients the blowing stands out as the best option.

To conclude, it is important to remark that there is a wide range of possibilities and parameters that can affect the performance of an Active Flow Control actuation at this ultra-low Reynolds regime and that there is not a unique solution able to perform with efficacy in different conditions. As a future work, it would be an interesting starting point to assess the influence of other parameters that would with certainty affect the results, such as the angle of attack, subharmonic frequencies for the synthetic jet case and moreover a 3D study to test the effectiveness in a realistic environment.

BIBLIOGRAPHY

[1] Sturm, Hannes. *"Boundary Layer Separation and Reattachment Detection on Airfoils by Thermal Flow Sensors". Sensors, 2012*: 14292-14306. ix, 3, 5

[2] LK Loftin Jr. *"Quest for Performance: The Evolution of Modern Aircraft" Part 2, chapter 10: High-Lift Systems*. NASA-SP-468, 1985. ix, 4

[3] Prabhakar and Ohri, "CFD Analysis on MAV NACA 2412 Wing in High Lift Take-Off Configuration for Enhanced Lift Generation". *J Aeronaut Aerospace Eng, 2:5, 7-8, 2013*. ix, 4

[4] T.Moghaddam and N.Neishabouri , "On the Active and Passive Flow Separation Control Techniques over Airfoils". *IOP Conf. Ser.: Master. Sci. Eng. 248 , 2017*. 5

[5] H. SCHLICHTING. *Boundary Layer Theroy*. (Frank J.Cerra. 1955)

[6] D.P. Jansen , "Passive Flow Separation Control on an Airfoil-Flap Model". *Delft University of Technology, 2012*. 5

[7] M.Jahanmiri, "Active Flow Control: A Review". *CHALMERS UNIVERSITY OF TECHNOLOGY, 2010*. 7, 8

[8] E. Graff, R. Seele, J. Lin I. Wygnanski, "Sweeping Jet Actuators - a New Design Tool for High Lift Generation". *51st AIAA Aerospace Sciences Meeting, 2013*. 7

[9] J.Winslow, H.Otsuka, B.Govindarajan and I.Chopra, "Basic Understanding of Airfoil Characteristics at Low Reynolds Numbers $(10^4–10^5)$". *AIAA JOURNAL OF AIRCRAFT, Vol. 55, No. 3, 2018*. 12

[10] D. Kurtulus, "On the Unsteady Behavior of the Flow Around NACA 0012 Airfoil with Steady External Conditions at Re=1000". *International Journal of Micro Air Vehicles, Vol. 7, No. 3, 2015*. 12

[11] "Impinging Sweeping Jet Heat Transfer". *53rd AIAA/SAE/ASEE Joint Propulsion Conference, 2017.* ix, 8, 9

[12] "Navier-Stokes Equations" *Glenn Research Center, NASA.* 21

[13] "COMPARISON OF CFD AND XFOIL AIRFOIL ANALYSES FOR LOW REYNOLDS NUMBER" *International Journal of Energy Applications and Technologies. Vol. 3, Issue 2, pp. 83 – 86, 2016.* 27

[14] "User guide 4.4.1". *Nektar++: Spectral/hp Element Framework*. Department of Aeronautics, Imperial College London, UK Scientific Computing and Imaging Institute, University of Utah, USA. 2017. 17, 22

[15] J.Mateu L.Colitti, "Sweeping-jet active flow control actuation effects on boundary layer separation on airfoil at ultralow Reynolds". *UPC, EETAC. 2019*. ix, 1, 29, 31, 32, 35

[16] C. Geuzaine and J.-F. Remacle. *Gmsh: a three-dimensional finite element mesh generator with built-in pre- and post-processing facilities. International Journal for Numerical Methods in Engineering 79(11), pp. 1309-1331, 2009. 17*

[17] https://es.mathworks.com/products/matlab.html 17

[18] https://www.paraview.org 17

[19] Skote, Martin Ibrahim, Imran Halimi. Utilizing the L-PSJA for controlling cylindrical wake flow. International Journal of Numerical Methods for Heat Fluid Flow. 26. 1593-1616. 2016. ix, 8

[20] Ramos Pedroza, Natalie Mackunis, William Reyhanoglu. A Sliding Mode LCO Regulation Strategy for Dual-Parallel Underactuated UAV Systems Using Synthetic Jet Actuators. International Journal of Aerospace Engineering. 2015. ix, 9